Bar-Ilan University

Tunable Flux Qubits with Long Coherence Times

Tamir Cohen

Submitted in partial fulfillment of the requirements for the Master's Degree in the

Department of Physics,

Bar-Ilan University

Ramat-Gan, Israel 2021

This work was carried out under the supervision of Dr. Michael Stern, Department of Physics, Bar-Ilan University

Contents

Abstract

The superconducting flux qubit is often considered as a strategic building block for the physical realization of quantum computers. It consists of a micron-size superconducting aluminum loop intersected by four Josephson junctions. It can be shown that such a circuit behaves as an almost ideal two-level system when the flux threading the loop is close to half a flux quantum. At the optimal point, precisely at half a flux quantum, the qubit is well protected from flux noise and its coherence time can reach few tens of microseconds [1–3].

A good control of the transition energy of the qubit at the optimal point is required if one wishes to build a scalable system. In this work, we replace one of the junctions by a SQUID. Adding a SQUID allows tuning the flux qubit's transition energy over a large range [4] but reduces the coherence times even at the optimal point. Here we propose to mitigate this problem by using an asymmetric SQUID, which is designed to control the qubit transition energy over a limited range while keeping long coherence times.

1 Background

1.1 Introduction

The discovery of the first quantum algorithms - such as Shor's factorizing algorithm [5], Grover's searching algorithm [6], and the error corrections protocol [7] - has triggered an intense experimental effort towards the physical realization of quantum computers. Among the various technologies, superconducting qubits have attracted a lot of attention due to their scalability and ease of use. These qubits consist of macroscopic electrical elements that can be easily coupled together via simple electrical elements like capacitors, inductors and transmission lines. Over the years, researchers have developed many different types of superconducting qubits architectures: Cooper pair boxes [8], quantronium [9], transmons [10], Xmons [11], flux qubits [1,12,13] and fluxonium [14].

The transmon qubits are today the most popular architecture for building superconducting quantum processors [15] [16], especially due to their long coherence times [10] and ease of use [17]. Yet, as one scales up the system, the large eigenvalue manifold of each transmon generates issues related to frequency crowding and gate fidelity. In contrast to transmons, flux qubits have intrinsically a huge anharmonicity: the higher energy levels of the system are very far from the qubit transition. Consequently, the flux qubit behaves as "true" two level systems, which limits frequency crowding issues. Moreover, they can be manipulated on a much shorter timescale and therefore could exhibit better gate fidelity. A good control of the transition energy of the qubit is required if one wishes to build a scalable system. The aim of the thesis is to solve this issue.

1.2 Josephson Relations

A circuit formed by linear components, such as capacitors and inductors, behaves as an harmonic oscillator and not as a qubit. A non-linear element is therefore essential in order to differentiate the transitions between states $|0\rangle$ and $|1\rangle$ from other higher-lying eigenstates transitions. In superconducting circuits, this non-linearity is obtained by adding to the circuit one or several Josephson junctions. Josephson junctions are formed by two superconducting islands separated by a thin insulating layer that allows tunneling of Cooper pairs. They are characterized by the so-called Josephson relations:

$$\begin{aligned} I &= I_0 \sin(\varphi) \\ V &= \varphi_0 \dot{\varphi} \end{aligned} \tag{1}$$

where φ it the phase difference between the two superconducting islands, I_0 is the critical current of the junction and φ_0 is the reduced magnetic flux quantum ($\hbar/2e$).

Josephson junctions are almost non-dissipative. This property allows their use in quantum circuits. The potential energy of the Josephson junction is given by:

$$E = \int_{-\infty}^{t} P dt' = \int_{-\infty}^{t} IV dt' = -E_J \cos(\varphi) \tag{2}$$

where $E_J = I_0 \varphi_0$ is called **Josephson energy**.

1.3 Introduction to superconducting flux qubits

Potential energy of the circuit

The superconducting flux qubit is a superconducting circuit which consists of a micron-size superconducting aluminum loop intersected by three, or more, Josephson junctions. In the following, we will consider the case of four junctions: all are identical except one which is smaller by a factor α as shown In Fig.1a.

The potential energy of the circuit can be written as a sum of the potential energies of each junction intersecting the loop (see Eqn.2).

A DC magnetic flux Φ is threading the circuit of the qubit, therefore due to Faraday law $\varphi_1+\varphi_2+\varphi_3+\varphi_\alpha = \frac{\Phi}{\varphi_0}$ and thus:

$$U = -E_J \left[\sum_{i=1}^{3} \cos(\varphi_i) + \alpha \cos(\frac{\Phi}{\varphi_0} - \varphi_1 - \varphi_2 - \varphi_3) \right] \tag{3}$$

When $\Phi/\varphi_0 = \pi$, the potential energy U exhibits two degenerated minima (Fig.1b), the potential barrier between these two minima being a function of the parameters of the junctions.

In order to determine the parameters of the circuit, we will first calculate the coordinates $(\varphi_1^*, \varphi_2^*, \varphi_3^*)$ of the minimal value of the potential energy when $\Phi/\varphi_0 = \pi$:

$$\begin{aligned} \frac{\partial U}{\partial \varphi_1} = 0 &\implies -\sin(\varphi_1^*) + \alpha \sin(\varphi_1^* + \varphi_2^* + \varphi_3^*) = 0 \\ \frac{\partial U}{\partial \varphi_2} = 0 &\implies -\sin(\varphi_2^*) + \alpha \sin(\varphi_1^* + \varphi_2^* + \varphi_3^*) = 0 \\ \frac{\partial U}{\partial \varphi_3} = 0 &\implies -\sin(\varphi_3^*) + \alpha \sin(\varphi_1^* + \varphi_2^* + \varphi_3^*) = 0 \end{aligned} \tag{4}$$

From Eqn.4 we get that $\varphi_1^* = \varphi_2^* = \varphi_3^* \, [2\pi]$ and $\sin(\varphi_{1,2,3}^*) = \pm\sqrt{\frac{3}{4} - \frac{1}{4\alpha}}$. These minima correspond to a **persistent current** flowing clockwise or anticlockwise in the loop of the qubit - denoted as I_p - and given by $I_P = I_0 \sin(\varphi^*) = \pm I_0 \sqrt{\frac{3}{4} - \frac{1}{4\alpha}}$.

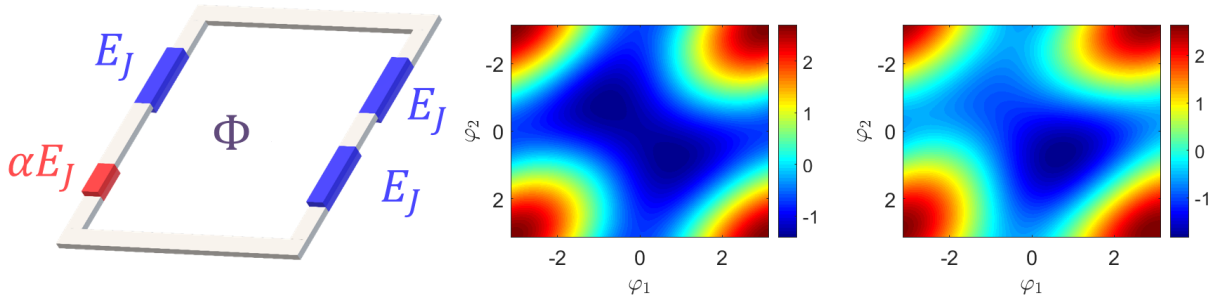

(a) (b) (c)

Figure 1: **(a)** 3D illustration of the flux qubit with four Josephson junctions. The unitary junction of Josephson energy E_J is represented in blue and the smaller junction of Josephson energy αE_J is represented in red. **(b-c)** Normalized potential energy of a 3-junction flux qubit as a function of the phases across junctions with two degenerated minima at $\Phi/\varphi_0 = \pi$ (b) and only one global minimum at $\Phi/\varphi_0 = 4\pi/5$ (c).

Hamiltonian of the circuit

In addition to its potential energy, the circuit Hamiltonian has a kinetic part which should be calculated in order to solve Schrodinger equation and get the eigenvalues and eigenstates of the system. To estimate it, one writes the Lagrangian of the circuit:

$$\mathcal{L} = \frac{1}{2}\varphi_0^2 C\left(\left(\dot{\varphi}_1^2 + \dot{\varphi}_2^2 + \dot{\varphi}_3^2 + \alpha(-\dot{\varphi}_1 - \dot{\varphi}_2 - \dot{\varphi}_3)^2\right) - U\right. \tag{5}$$

The conjugate momenta q_i of the variable φ_i are defined by:

$$q_i = \frac{\partial \mathcal{L}}{\partial \dot{\varphi}_i} = \varphi_0^2 C\left((1+\alpha)\,\dot{\varphi}_i + \alpha\dot{\varphi}_{i+1[3]} + \alpha\dot{\varphi}_{i+2[3]}\right) \tag{6}$$

The Hamiltonian is given by $\mathcal{H} = \sum_i \dot{\varphi}_i q_i - \mathcal{L}$ which gives[1]:

[1] The general expression for the kinetic part of a circuit intersected by 4 different Josephson junctions ,r_i is give by:
$\frac{4E_C}{r_1r_2r_3+r_4(r_1r_2+r_1r_3+r_2r_3)}\left[n_1^2\left(r_2r_3+r_2r_4+r_3r_4\right)+n_2^2\left(r_1r_3+r_1r_4+r_3r_4\right)+n_3^2\left(r_1r_2+r_1r_4+r_2r_4\right)-2r_4\left(n_2n_3r_1+n_1n_3r_2+n_1n_2r_3\right)\right]$

$$\mathcal{H} = \frac{4E_C}{1+3\alpha}\left((1+2\alpha)\sum_{i=1}^{3} n_i^2 - \alpha\sum_{i=1}^{3}\sum_{j\neq i}^{3} n_i n_j\right) + U \tag{7}$$

where $n_i = q_i/(2e)$ represents the number of Copper pairs tunneling via the junction i such that $[\varphi_i, n_i] = \mathbf{i}$ and $E_C = \frac{e^2}{2C}$. In order to solve the Hamiltonian we project it into the charge basis where $\hat{n}_i |m\rangle = m|m\rangle$ and $\cos\hat{\varphi}_i |m\rangle = \left(e^{i\hat{\varphi}_i}|m\rangle + e^{-i\hat{\varphi}_i}|m\rangle\right)/2$. In that basis, the operator $\hat{n}_i$ is diagonal and $\cos(\hat{\varphi}_i)$ is sparse :

$$\cos(\hat{\varphi}_i) = \frac{1}{2}\begin{bmatrix} 0 & 1 & 0 & \cdots & 0 \\ 1 & 0 & 1 & \ddots & \vdots \\ 0 & 1 & 0 & \ddots & 0 \\ \vdots & \ddots & \ddots & \ddots & 1 \\ 0 & \cdots & 0 & 1 & 0 \end{bmatrix} \tag{8}$$

In Fig.2a the first four eigenenergies are presented as a function of the external magnetic flux Φ threading the loop. In the vicinity of $\Phi/\varphi_0 = \pi$, the system behaves as an almost ideal two level system: the two lowest energy levels are far from the higher levels. The transition energy between the first excited state and the ground state of the system at $\Phi/\varphi_0 = \pi$ is called **flux qubit gap** and is denoted as Δ. The value of Δ is given by the tunneling probability between the two degenerate minima of the potential energy (see Fig.1b).

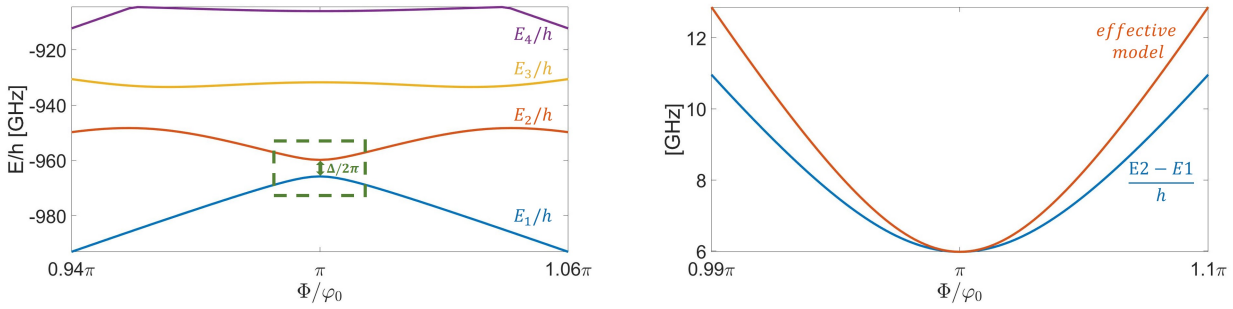

(a) (b)

Figure 2: **(a)** Four first energy levels of a flux qubit as a function of Φ. The energy difference $E_3 - E_2$ is much higher than $E_2 - E_1$. Therefore, the qubit can be treated as a two level system. **(b)** $E_2 - E_1$ in blue and the effective model of the qubit in red as a function of Φ/φ_0. The approximation of the effective model is correct only in the vicinity of $\Phi/\varphi_0 = \pi$.

Effective Hamiltonian

As mentioned above, the system should behave as a two level system in the vicinity of $\Phi/\varphi_0 = \pi$. In this region, the Hamiltonian of the system can be written using perturbation theory as:

$$\begin{aligned} \mathcal{H} &= H_0 - \alpha E_J \partial_\Phi \left(\cos(2\pi\tfrac{\Phi}{\Phi_0} - \textstyle\sum_i \varphi_i)\right)_{\Phi=0.5\Phi_0} \cdot \left(\Phi - \tfrac{\Phi_0}{2}\right) \\ &= H_0 + \tfrac{1}{\varphi_0}\left[\underbrace{\alpha E_J \sin(\varphi_\alpha)}_{\hat{I}\cdot\varphi_0}\left(\Phi - \tfrac{\Phi_0}{2}\right)\right] = H_0 + \hat{I}\left(\Phi - \tfrac{\Phi_0}{2}\right) \end{aligned} \tag{9}$$

When the current operator is projected on the eigenstates $|g\rangle, |e\rangle$ of H_0 we get:

$$\begin{aligned} \langle g|\hat{I}|g\rangle = 0 \quad , \quad \langle g|\hat{I}|e\rangle = I_p \\ \langle e|\hat{I}|g\rangle = I_p \quad , \quad \langle e|\hat{I}|e\rangle = 0 \end{aligned} \tag{10}$$

Therefore, the Hamiltonian of the system can be written in this basis as:

$$\mathcal{H}_{eff} = \frac{\hbar}{2}\left[\Delta\sigma_z + \varepsilon\sigma_x\right] \tag{11}$$

where $\varepsilon = \frac{2I_p}{\hbar}\left(\Phi - \frac{\Phi_0}{2}\right)$.

When $\varepsilon \neq 0$ one can write the Hamiltonian as a function of the so-called mixing angle $\theta = \text{atan}(\varepsilon/\Delta)$and it becomes:

$$\mathcal{H}_{eff} = \omega_{ge}\left[\cos(\theta)\sigma_z + \sin(\theta)\sigma_x\right]$$

where $\omega_{ge} = \sqrt{\Delta^2 + \varepsilon^2}$ is the 11 transition frequency between the two eigenstates $|g'\rangle$, $|e'\rangle$ that are given by:

$$\begin{array}{l} |g'\rangle = \cos(\theta/2)|g\rangle + \sin(\theta/2)\,|e\rangle \\ |e'\rangle = sin(\theta/2)\,|g\rangle - \cos(\theta/2)\,|e\rangle \end{array} \tag{12}$$

1.4 Flux Qubit Measurements techniques

In the following, we will briefly describe two different techniques usually used to perform the readout of a flux qubit.

DC- SQUID Readout

The first technique for reading out flux qubits consists of using a SQUID in the configuration shown In Fig.3b. The SQUID can be considered as a tunable Josephson junction with a tunable critical current given by $I_{sq} = 2I_0\left|\cos\left(\frac{\Phi_s}{2\varphi_0}\right)\right|$, where I_0 is the critical current of the junctions, which form the SQUID and Φ_s is the flux threading the loop of the SQUID.

As shown on Fig.3a , a SQUID is fabricated around the flux qubit. That architecture is chosen in order to maximize the SQUID sensitivity to the magnetic flux generated by the persistent current I_p of the qubit. A DC current I_{bias} is applied on the detecting SQUID. In such a configuration, the potential energy of the detecting SQUID has a shape of a washboard and can be written as [18–20]:

$$U_{sq}(\varphi) = -I_{sq}\varphi_0\cos(\varphi) - I_{bias}\varphi_0\varphi \tag{13}$$

When I_{bias} is below the critical current of the SQUID ($I_{bias} < I_{sq}$), the washboard potential has minimas such that $\dot{\varphi} = 0$ and therefore no potential drop V_{sq} is observed. However, when the bias current is above I_{sq}, the potential energy has no minimas and the phase will start moving down the washboard potential: a DC voltage V_{sq} appears.

The probability to switch between these two states depends on the value of the bias current as shown In Fig.3c and on the state of the qubit (gray lines). When one apply a rectangular pulse current, the switching probability can be described as:

$$P_{sw}(I_{bias}, \tau_m) = 1 - e^{-\Gamma(I_{bias})\tau_m} \tag{14}$$

where τ_m is the measurements pulse duration (see Fig 3b).

This probability depends on whether the qubit is in a state where the current flowing in its loop is rotating anticlockwise ($|L\rangle = \frac{|g\rangle+|e\rangle}{\sqrt{2}}$), or in a state where the current is flowing clockwise ($|R\rangle = \frac{|g\rangle-|e\rangle}{\sqrt{2}}$). Therefore the state of the qubit can be determined by the switching statistics.

This technique presents a major disadvantage: the dissipative current produced by the SQUID generates heat in the vicinity of the qubit and may modify the probability to have a false switching by thermal excitations.

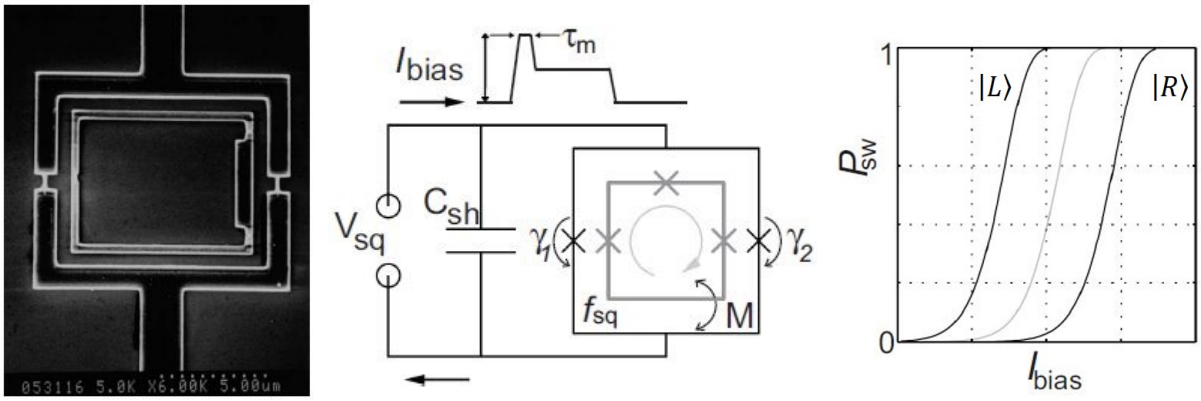

(a) (b) (c)

Figure 3: **(a)** SEM micrograph of flux qubit (inside) and DC-SQUID (outside), taken from [21, 22]). The Josephson junctions are located the constricted regions both in the qubit (three junctions) and the SQUID (two junctions). **(b)** Schematic drawing of the readout circuit, taken from [23]. A current pulse of amplitude I_{bias} with a typical pulse duration τ_m is applied into the measurement DC-SQUID. The amplitude of this pulse is close to the critical current $I_{c,sq}$, such that the probability of switching event depends rather the qubit is in $|L\rangle$ or $|R\rangle$ state - the switching events produce voltage drops that can be measured. The SQUID is shunted with a capacitor C_{sh} to control the plasma frequency that effects the switching statistics. **(c)** An histogram of the switching probability as a function of the bias current I_{bias}that flows in the DC-SQUID. The gray line represents the probability where there is no qubit inside the DC-SQUID. This probability changes whether the qubit is in his $|L\rangle$ or $|R\rangle$ states for a given current I_{bias}. When the qubit is in $|L\rangle$ state small currents are needed to switch the state of the qubit. Therefore, by knowing the value of I_{bias} when a switch event occurred, one knows with some probability the state of the qubit.

Circuit QED Readout

The second technique for reading out flux qubits consists of using a superconducting resonator in the configuration shown in Fig.4a. The flux qubit is coupled inductively to the resonator such that its coupling energy with the resonator is given by:

$$\mathcal{H}_{int} = M\hat{I}_R\hat{I} \tag{15}$$

where M is the mutual inductance between the flux qubit and the resonator, $\hat{I}_R$ is the current operator flowing in the resonator and $\hat{I}$ the current operator of the qubit.

The current operator inside the resonator $\hat{I}_R$ is given by $\hat{I}_R = \delta I_0\left(a + a^\dagger\right)$, where $a^\dagger$ and a are the creation and the annihilation operators respectively, $\delta I_0 = \omega_r\sqrt{\hbar/2Z_0}$ is the amplitude of the current fluctuations inside the resonator ω_r is the resonance frequency and Z_0 is the characteristic impedance of the resonator. The current of the qubit , as shown in Eqn.10, can be written as $\hat{I} = I_p\hat{\sigma}_x = I_p\left(\sigma^+ + \sigma^-\right)$.

Finally, the interaction term can be written as:

$$\mathcal{H}_{int} = \hbar g(a + a^\dagger)(\sigma^+ + \sigma^-) \tag{16}$$

where $g = \frac{MI_p\delta I_0}{\hbar}$ is the coupling constant.

The terms $\sigma^+a^\dagger$ and σ^-a do not conserve the number of excitations and can be neglected if the detuning $\Delta_R = \omega_{ge} - \omega_r$ between the qubit and the resonator is small enough $\Delta_R \ll \omega_r, \omega_{ge}$ [24]. Therefore, one can simplify the interaction term to the so-called the Jaynes-Cummings interaction. The total Hamiltonian of the qubit resonator system can therefore be written as:

$$\mathcal{H} = \hbar\omega_r\left[aa^\dagger + \frac{1}{2}\right] + \frac{\hbar}{2}\left[\Delta\sigma_z + \varepsilon\sigma_x\right] + \hbar g(a^\dagger\sigma^- + a\sigma^+) \tag{17}$$

The eigenenergies of this system are:

$$E_n^\pm = (n + 1/2)\,\hbar\omega_r \pm \frac{\hbar}{2}\sqrt{\Delta_R^2 + 4g^2\,(n+1)} \tag{18}$$

where n is the number of photons inside the resonator.

The eigenstates of the system are:

$$\begin{aligned} |+,n\rangle &= -\cos(\theta_n/2)|e,n\rangle + \sin(\theta_n/2)\,|g,n+1\rangle \\ |-,n\rangle &= \sin(\theta_n/2)\,|e,n\rangle + \cos(\theta_n/2)\,|g,n+1\rangle \end{aligned} \tag{19}$$

where $\theta_n = \text{atan}(2g\sqrt{n+1}/\Delta_R)$ in the mixing angle.

In the limit where the detuning is large in front of g ($\Delta_R \gg g$), the eigenenergies of the system can be simplified up to first order as:

$$E_n^{\pm} = (n+1/2)\,\hbar\omega_r \pm \hbar\left(\frac{\Delta_R^2}{2} + \frac{g^2\,(n+1)}{\Delta_R}\right) \tag{20}$$

As a consequence, the energy of the resonator shifts whether the qubit is in its ground state or excited state. These frequency shifts Δ_e and Δ_g (see Fig.4b) are given by:

$$\Delta_g = \frac{E_{n+1}^{+} - E_n^{+}}{\hbar} = \frac{g^2}{\Delta_R} \tag{21}$$

$$\Delta_e = \frac{E_{n+1}^{-} - E_n^{-}}{\hbar} = -\frac{g^2}{\Delta_R} \tag{22}$$

It is therefore possible to measure the state of the qubit by measuring the resonance frequency of the resonator. A simple way to perform this measurement consists of applying a microwave tone ω_{meas} close to the resonance frequency of the resonator and measuring its transmission. The phase and the intensity of the output signal are respectively given by the input-output theory [25] by:

$$\angle S_{21}(f) = -\arctan\left(2Q_{tot}\frac{\omega_{meas}-\omega_r}{\omega_r}\right) \tag{23}$$

$$|S_{21}(f)|^2 = \left(\frac{Q_{tot}}{Q_c}\right)^2 \frac{1}{1+4Q_{tot}^2\left(\frac{\omega_{meas}-\omega_r}{\omega_r}\right)^2} \tag{24}$$

where Q_{tot} is the total quality of the resonator and $Q_c$the one which is due to its coupling with external lines.

This technique presents several advantages. First, it is possible to measure several qubits with the same detecting system [1].Second it is a Quantum Non-Demolition (QND) measurement. During the measurement information about the system is preserved such that it is projected to an corresponding eigenstate of the measurement. Furthermore, no heat is generated during the process which allows repeating the measurement many time without modifying the state of the qubit due to thermal excitations [26, 27].

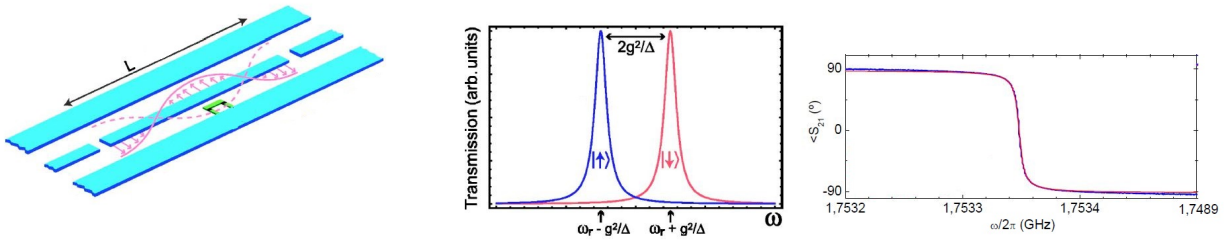

(a) (b) (c)

Figure 4: **(a)** Schematic layout and equivalent lumped circuit representation of proposed implementation of cavity QED using superconducting circuits, the flux qubit is placed between the superconducting lines and is coupled to the center conductor at a maximum of the current of the standing wave, yielding a strong magnetic dipole interaction between the qubit and a single photon in the cavity. **(b)** The resonance frequency shifts by $\pm\frac{g^2}{\Delta_R}$ due to the the state of the qubit $|e\rangle$, $|g\rangle$. **(c)** A phase shift of the transmitted signal through the resonator. All the figures were taken from [25].

1.5 Coherence Time Limitations

Intrinsic relaxation rate

The relaxation of the flux qubit is due to several mechanisms. Quasiparticles in the superconducting loop are in general considered as one of the major channel of relaxation. These quasiparticles exist even at low temperatures. They give rise to a relaxation rate of the qubit which is directly proportional to their density [1,28–32]. Another mechanism for relaxation is related to dielectric losses in the Josephson junctions or in the substrate. It was shown in Ref. [33] that the value of $\tan\delta_{JJ}$ for losses in the Al_2O_3 barrier of the junction is typically in the range of $3 \cdot 10^{-7}$ while $\tan\delta_{substrate}$ [34] is typically much larger $\sim 2 \cdot 10^{-5}$. This last value gives rise to a typical relaxation time $T_1 \sim 20\mu s$ [35].

Relaxation due to surrounding cavity : Purcell effect

Another mechanism of relaxation is due to the coupling of the qubit with its readout resonator - the so-called Purcell effect. This effect represents the spontaneous emission of the qubit to the environment via the resonator (see Fig 5).

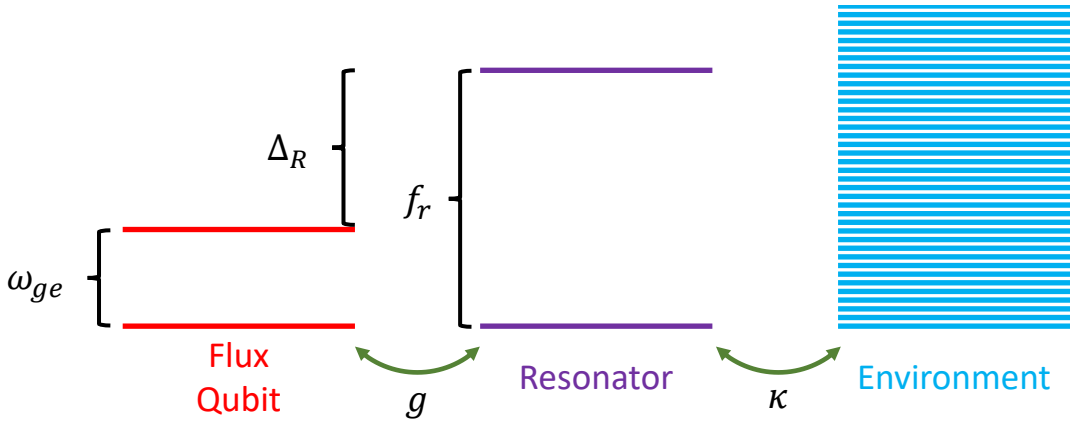

Figure 5: Scheme representing Purcell relaxation mechanism. The energy levels of the qubit (resp. resonator) are represented in red (resp. purple). The environment contiumum is shown in blue. The qubit and the resonator are coupled by coupling constant g. The resonator is coupled via its ports with a loss rate κ to the environment.

The qubit and the resonator are inductively coupled by coupling constant g as presented in Sec.1.4. In addition the resonator is also coupled the external ports, with a loss rate $\kappa \sim \omega_r/Q$.

The rate of decay of an eigenstate of the system shown in Eqn.19 is simply given by:

$$\Gamma_{tot} = \cos^2(\theta_n/2) \cdot \gamma + \sin^2(\theta_n/2) \cdot \kappa$$

where γ is the intrinsic relaxation rate of the qubit. The second term of this expression corresponds to the so-called Purcell rate Γ_P. When θ_n is small, $\sin^2(\theta_n) \sim g^2/\Delta^2$ and therefore $\Gamma_P = g^2/\Delta^2 \cdot \kappa$.

It is possible to relate Γ_P to the Rabi frequency of the qubit at a given power P_{in} by noting that $\Omega_R = 2g\sqrt{\bar{n}}$ where $\bar{n}$ corresponds to the average number of photons at the frequency of the qubit in the resonator. This number of photons is given by input output theory [36–38] and is given by:

$$\bar{n} = \frac{\kappa P_{in}}{2\Delta_r^2 \hbar\omega_{ge}} \tag{25}$$

Using this expression we get that

$$\boxed{\Gamma_p = \frac{\Omega_R^2 \hbar\omega_{ge}}{2\,P_{in}}} \tag{26}$$

Pure dephasing rate

In an ideal system, the decoherence rate Γ_2 is limited by the energy relaxation rate of the qubit and is given by: $\Gamma_2 = \Gamma_1/2$ [39]. In practice, the decoherence rate of a qubit may be much larger than this theoretical limit. There are several known sources of dephasing which are responsible for this. Among them, flux noise [2] , charge noise [1], photon noise in the resonator [40]. The pure dephasing rate of the qubit can be estimated by the so-called Ramsey sequence, where two identical $\pi/2$ pulses are played consequently with a time interval t. It is possible to dynamically decouple the noise responsible for this dephasing by playing a more complex set of pulses. The most popular technique to achieve this is called Hahn Echo technique and consists of playing a π-pulse in between the two $\pi/2$ pulses. This π pulse inverses the time evolution and therefore cancels the contribution to dephasing of low frequency noise. As we will see hereinbelow, the noises at high frequency cannot be reduced by this technique and therefore the comparison of Ramsey and Echo dephasing rates gives us a way to better understand the noise power spectrum.

Ramsey sequence

The first $\pi/2$-pulse raises the qubit initially in its ground state into a coherent superposition of $|\Psi(0)\rangle = (|g\rangle + |e\rangle)/\sqrt{2}$. During time t, the qubit performs a free evolution and accumulates phase $\varphi(t)$ and becomes $\Psi(t) = \left(|g\rangle + e^{i\varphi(t)}|e\rangle\right)/\sqrt{2}$.

The phase $\varphi(t)$ consists of two parts $\varphi(t) = \omega_{ge}t + \delta(t)$, where $\delta(t)$ is the phase due to the small fluctuations $\delta\lambda(t)$ which slightly modify the qubit Hamiltonian. At first order, $\delta(t)$ is given by $\delta(t) = \frac{\partial\omega_{ge}}{\partial\lambda}\int_0^t \delta\lambda(t')dt'$.

The decoherence rate of the system corresponds to the decay of the expectation value $\langle\sigma_x(t)\rangle$ and is given by [41]:

$$\langle\sigma_x(t)\rangle = 1/2\,(e^{i\varphi(t)} + e^{-i\varphi(t)})$$

When repeating the measurements, the value of $\langle\sigma_x(t)\rangle$ is changed due to the varying environmental noise $\delta(t)$. Therefore, one should average the value of of $e^{\pm i\delta(t)}$ in order determine the influence of this noise. If the fluctuations $\delta\lambda(t')$ are small enough, they can be considered as a random variable with Gaussian distribution[2]. Thus:

$$f_R(t) = \left\langle e^{\pm i\delta(t)}\right\rangle \approx \left\langle 1 \pm \cancel{i\delta} - \delta^2/2\right\rangle = e^{-1/2\langle\delta^2\rangle}$$

The expectation value of $\langle\sigma_x(t)\rangle$ will therefore decay according to:

$$f_R(t) = e^{-1/2\left(\frac{\partial\omega_{ge}}{\partial\lambda}\right)^2\left\langle\left(\int_0^t \delta\lambda(t')dt\right)^2\right\rangle} = \exp\left(-\frac{t^2}{2}\left(\frac{\partial\omega_{ge}}{\partial\lambda}\right)^2 \int_{-\infty}^{\infty} d\omega\, S_\lambda(\omega)\,\mathrm{sinc}^2(\frac{\omega t}{2})\right) \tag{27}$$

Where $S_\lambda(\omega) = 1/2\pi\int_{-\infty}^{\infty}\langle\lambda(t)\lambda'(t+\tau)\rangle\exp(-i\omega t)dt$.

Hahn Echo sequence

Like in the Ramsey sequence, the first $\pi/2$-pulse puts the state of the qubit in a coherent superposition state $|\Psi(0)\rangle = (|g\rangle + |e\rangle)/\sqrt{2}$. During the time t_1, the qubit performs a free evolution and accumulates phase $\varphi_1(t_1) = \omega_{ge}t_1 + \delta_1(t_1)$. The π - pulse flips the time evolution of the qubit such that during the time t_2 it acquires an opposite phase $\varphi_2(t_2) = -\omega_{ge}t_2 - \delta_2(t_2)$.

The phase accumulated by $\omega_{ge}t_1$ and $\omega_{ge}t_2$ is canceled when $t_1 = t_2 = t/2$ and the decoherence rate of the qubit - corresponding to the decay $f_E(t) = \langle\sigma_x(t)\rangle$ - is given by:

$$f_E(t) = \left\langle e^{\pm i(\delta_1 - \delta_2)}\right\rangle \approx \exp\left(-1/2\left\langle\delta_1^2 + \delta_2^2 - \delta_1\delta_2 - \delta_2\delta_1\right\rangle\right)$$

The expectation value of $\langle\sigma_x(t)\rangle$ will therefore decay according to:

$$f_E(t) = \exp\left(-\frac{t^2}{2}\left(\frac{\partial\omega_{ge}}{\partial\lambda}\right)^2 \int_{-\infty}^{\infty} d\omega\, S_\lambda(\omega)\sin^2(\frac{\omega t}{4})\,\mathrm{sinc}^2(\frac{\omega t}{4})\right)$$

[2]The average of δ is zero due to the this assumption.

White & $1/f$ noise

In the previous sections we showed that $f_R(t)$ and $f_E(t)$ are functions of the noise spectrum $S_\lambda(\omega)$. In the following we will present the dephasing rate of the qubit due to some usual noise power spectra, namely white noise and $1/f$ noise.

1. **White noise:**

   In that case, we assume that $S_\lambda(\omega) = S_\lambda(\omega = 0)$ is a constant.

   Therefore, the Ramsey decay is given by:

$$f_R(t) = \exp\left(-\frac{t^2}{2}\left(\frac{\partial\omega_{ge}}{\partial\lambda}\right)^2 S_\lambda(\omega=0)\int_{-\infty}^{\infty} d\omega\,\mathrm{sinc}^2(\frac{\omega t}{2})\right)$$

   Since $\int_{-\infty}^{\infty}\mathrm{sinc}^2(\omega t/2)d\omega = 2\pi/t$, $f_R(t)$ decays exponentially at a rate Γ_{2R}^w given by:

$$\boxed{\Gamma_{2R}^w = \pi S_\lambda(\omega=0)\left(\frac{\partial\omega_{ge}}{\partial\lambda}\right)^2}$$

   The Echo decay is given by:

$$f_E(t) = \exp\left(-\frac{t^2}{2}\left(\frac{\partial\omega_{ge}}{\partial\lambda}\right)^2 S_\lambda(\omega=0)\int_{-\infty}^{\infty} d\omega\,\sin^2(\frac{\omega t}{4})\,\mathrm{sinc}^2(\frac{\omega t}{4})\right)$$

   Since $\int_{-\infty}^{\infty}\sin^2(\omega t/4)\ \mathrm{sinc}^2(\omega t/4) = 2\pi/t$, we obtain also an exponential decay , where Γ_{2E}^w is given by:

$$\boxed{\Gamma_{2E}^w = \pi S_\lambda(\omega=0)\left(\frac{\partial\omega_{ge}}{\partial\lambda}\right)^2}$$

   Hence, the Echo and the Ramsey sequences decay at the same rate.

2. $1/f$ **noise:**

   The noise power spectrum is such that $S_\lambda(\omega) = A/|\omega|$. Therefore, the Ramsey decay is given by:

$$f_R(t) = \exp\left(-\frac{t^2}{2}\left(\frac{\partial\omega_{ge}}{\partial\lambda}\right)^2\int_{-\infty}^{\infty} d\omega\,\frac{A}{|\omega|}\,\mathrm{sinc}^2(\frac{\omega t}{2})\right)$$

   since:

$$\int_{-\infty}^{\infty}\frac{d\omega}{|\omega|}\,\mathrm{sinc}^2(\frac{\omega t}{2}) = 2\cdot\int_0^{\infty}\frac{d\omega}{\omega}\,\mathrm{sinc}^2(\frac{\omega t}{2}) \approx 2\cdot\int_{\omega_{ir}}^{\omega_c}\frac{d\omega}{\omega}\,\mathrm{sinc}^2(\frac{\omega t}{2}) \approx 2\cdot ln(\frac{1}{\omega_{ir}t})$$

   where $\omega_c \sim 1MHz$ and $\omega_{ir} \sim 1$Hz. Therefore, we get that $f_R(t) = \exp\left[-\left(t\Gamma_{2,R}^{1/f}\right)^2\right]$ is Gaussian and the Ramsey dephasing rate is:

$$\boxed{\Gamma_{2R}^{1/f} = \left(\frac{\partial\omega_{ge}}{\partial\lambda}\right)\sqrt{A\ln\frac{1}{\omega_{ir}t}}} \tag{28}$$

   For Echo decay, the integral $\int_{-\infty}^{\infty} d\omega\,\frac{A}{|\omega|}\sin^2(\frac{\omega t}{4})\,\mathrm{sinc}^2(\frac{\omega t}{4}) = \ln(2)$ and therefore $f_E(t) = \exp\left[-\left(t\Gamma_{2,E}^{\varphi}\right)^2\right]$ is also Gaussian where $\Gamma_{2,E}^{1/f}$ is given by:

$$\boxed{\Gamma_{2E}^{1/f} = \left(\frac{\partial\omega_{ge}}{\partial\lambda}\right)\sqrt{A\ln 2}} \tag{29}$$

For a typical coherence times in the range of $t = 1\mu$s the ratio of the decoherence between Ramsey and Echo dephasing rates is:

$$R_{R/E} = \frac{\Gamma_{2R}^{\varphi}}{\Gamma_{2E}^{\varphi}} \approx 4.5$$

In our system, the main source of $1/f$ noise is the so-called flux noise.

$$\frac{\partial\omega_{ge}}{\partial\Phi} = \frac{\partial\omega_{ge}}{\partial\varepsilon} \times \frac{\partial\varepsilon}{\partial\Phi} = \varepsilon/\sqrt{\varepsilon^2+\Delta^2} \times \frac{2I_p}{\hbar}$$

At $\Phi/\varphi_0 = \pi$, $\varepsilon = 0$, thus, the derivative $\partial\omega_{ge}/\partial\Phi$ is equal to zero and therefore the qubit is immune to flux noise up to first order. For this reason the point at which $\Phi/\varphi_0 = \pi$ is called the **optimal point**.

Far away from the optimal point ($\varepsilon \gg \Delta$), $\frac{\partial\omega_{ge}}{\partial\Phi} = 2I_p/\hbar$. Assuming, $I_p \sim 0.5\mu A$ and $A = 2\mu\Phi_0$ we get:

$$\begin{array}{c} \Gamma_{2R} \sim 30\,MHz \\ \Gamma_{2E} \sim 6.5\,MHz \end{array} \tag{30}$$

The coherence time of the flux qubit away from its optimal point is extremely short. Therefore, one must work as close as possible to the optimal point if one wishes to get a long coherence time. Yet, the frequency of the qubit at this point is difficult to control. In the following paragraph, we will explain how we wish to control the qubit frequency while keeping long coherence times.

2 Methodology

As already mentioned, the flux qubit gap energy $\hbar\Delta$ is given by the tunneling probability between the two degenerate minima of its potential energy. Using W.K.B approximation [42], it is possible to estimate the value of Δ [43]:

$$\Delta \propto \exp\left[-\frac{2}{\hbar}\int_{-\varphi^*}^{\varphi^*}\left|\sqrt{2m_{eff}\cdot\Delta U(\varphi)}\right|d\varphi\right]$$

where $m_{eff} = 2C\varphi_0^2(1+2\alpha)$, $\Delta U(\varphi) = U(\varphi) - U(\varphi^*)$, φ^* being the phase of the degenerate minimum. In the simple case of a three junction qubit $\Delta U(\varphi)$=$(\cos\varphi - 1/2\alpha)^2$. Therefore, by integrating the expression herein above we get:

$$\Delta \propto \exp\left[-\left|\sin\varphi^* - \frac{\varphi^*}{2\alpha}\right|\sqrt{4\alpha(1+2\alpha)\frac{E_J}{E_C}}\right]$$

We see clearly that the gap is exponentially dependent on the parameters of the junctions (E_J,E_C, α). A slight change of these parameters will affect drastically the gap energy of the qubit. In addition to this, the Josephson energy E_J of the junctions is known to be exponentially dependent on the width of the oxide which separate the two superconducting islands of the junction [19].

If one wishes to control precisely the gap energy, a good strategy may consist of replacing one of the junction by a SQUID, which will act as a tunable junction. The advantage of this approach is that another degree of freedom is added to the system; the flux Φ_S in the loop of the SQUID. Φ_S controls the critical current of the tunable junction formed by the SQUID and thus allows controlling the energy of the flux qubit while keeping it at its optimal point. In Ref. [4], this kind of strategy was implemented: a symmetric SQUID was introduced at the position of the α-junction of the flux qubit in order to control its gap energy. The results of the experiments were positive in terms of control of the qubit gap but the coherence times of the

qubit **even at optimal point** were rather poor. The origin of these extremely short coherence times relates to the presence of flux noise in the SQUID loop, which leads to energy fluctuations even at the optimal point.

In this thesis, we would like to study how to control the gap of the flux qubit, while keeping its coherence time in the range of a few microseconds.

2.1 SQUID's Potential Energy

It should be possible to get some control of the qubit gap by using a highly asymmetric SQUID that will replace one of the unitary junctions, as shown in Fig.6a. In the following section we will show how the asymmetry of the SQUID allows controlling its Josephson energy via the magnetic flux threading the loop of the SQUID Φ_S. First, let us write the potential energy U_S of the asymmetric SQUID, Fig.6b:

$$U_S = -\frac{1+d}{2}E_J\cos(\varphi_1) - \frac{1-d}{2}E_J\cos(\varphi_2) \tag{31}$$

where d is the asymmetry parameter ,which can get any value in range of $\{0,1\}$. A DC magnetic flux Φ_S is threading the loop of the SQUID such that $\varphi_1 - \varphi_2 = \frac{\Phi_S}{\varphi_0}$ leading to:

$$U_S = \underbrace{-E_J\sqrt{\frac{(1+d^2)+(1-d^2)\cos\left(\frac{\Phi_s}{\varphi_0}\right)}{2}}}_{E_J\cdot\beta(\Phi_S)}\cdot\cos\left(\underbrace{\frac{\varphi_1+\varphi_2}{2}+\arctan\left[-d\cdot\tan\left(\frac{\Phi_s}{2\varphi_0}\right)\right]}_{\varphi_3}\right) \tag{32}$$

The potential energy of the SQUID is therefore equivalent to the potential energy of a *single* Josephson junction with tunable Josephson energy $E_J\cdot\beta(\Phi_S)$ that varies between dE_J to E_J, as shown in Fig.6c. When the assymetry is large ($d \lesssim 1$), the Josephson energy of the SQUID varies slightly. Therefore, it will be less sensitive to flux noise than for a symmetric SQUID ($d = 0$).

2.2 Tunability of the Flux Qubit

The introduction of the asymmetric SQUID presented in previous section allows tuning the flux qubit gap Δ on a large range. In the following, we calculate this range by writing the new potential energy of the system and diagonalizing the Hamiltonian. At the optimal point, the potential energy of the tunable flux qubit can be written as:

$$U(\varphi_1,\varphi_2,\varphi_3,\Phi_S) = -E_J\left[\cos(\varphi_1)+\cos(\varphi_2)+\beta(\Phi_S)\cos(\varphi_3)-\alpha\cos(\varphi_1+\varphi_2+\varphi_3)\right] \tag{33}$$

The kinetic part of the Hamiltonian remains unchanged. The total Hamiltonian of the qubit is therefore given by:

$$\mathcal{H} = \frac{4E_C}{1+3\alpha}\left((1+\alpha)\sum_{i=1}^{3}n_i^2 - \alpha\sum_{i=1}^{3}\sum_{j\neq i}^{3}n_in_j\right) + U(\varphi_1,\varphi_2,\varphi_3,\Phi_S) \tag{34}$$

In Fig.7a we represented the transition frequency of three qubits with different asymmetric SQUIDs. As expected, the tunability of the flux qubit gap increases strongly when d decreases. An asymmetric SQUID with $d = 0.75$ is enough to be able to control the qubit gap on a range of $\sim 3\,\mathrm{GHz}$. The gap of the qubit behaves as:

$$\boxed{\Delta(d,\Phi_S) = \Delta_0 + \delta(d)\cos\Phi_S/\varphi_0}$$

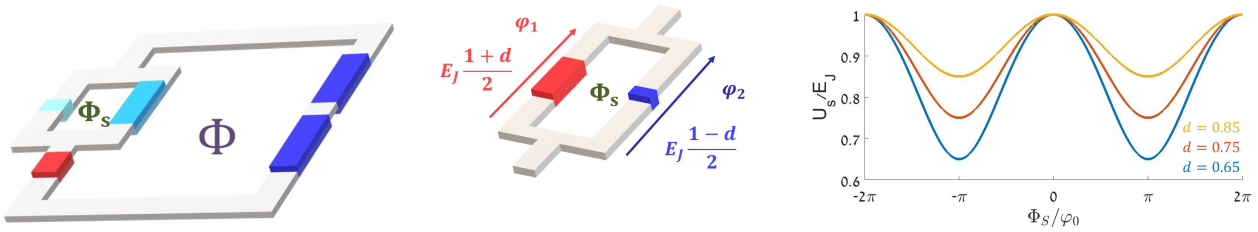

(a) (b) (c)

Figure 6: **(a)** A 3D illustration of the SQUID that replaces one of the qubits junction. **(b)** A 3D illustration of the asymmetric SQUID. **(c)** Effective potential energy of the SQUID for different asymmetric parameters $d = 0.65$, $d = 0.75$, $d = 0.85$.The tunability increases while d decreases.

2.3 Coherence Time

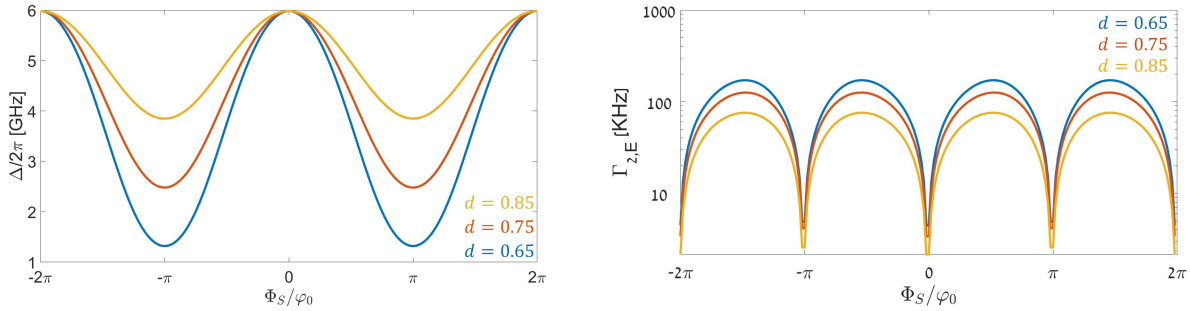

(a) (b)

Figure 7: **(a)** The tunability of the three tunable flux qubits intersected by different asymmetric SQUID $d = 0.65$, $d = 0.75$, $d = 0.85$ as a function of the flux threading the SQUID loop. The tunability of the flux qubit gap increases strongly when d decreases. **(b)** The effect of the first order flux noise caused by the flux threads the loop of the different asymmetric SQUIDs as a function of the flux threading it. The coherence time increases with the increase of d.

The coherence time of the system will be most likely dominated by first order flux noise inside the SQUID loop. In the following, we calculate the pure dephasing time of our system due to flux noise in the SQUID. This calculation was done using the approach described in Sec.1.5. Using the results herein above, the Echo decoherence rate is given by:

$$\boxed{\Gamma_{2E} = \delta(d)\left|\sin\frac{\Phi_S}{\varphi_0}\right|\frac{\sqrt{A\ln(2)}}{\varphi_0}} \tag{35}$$

The decay rate $\Gamma_{2,E} \sim 100$KHz, where $\delta(d) = 2\pi \times 1.5$GHz, $\sqrt{A} = 2\,\mu\Phi_0$ and $\Phi_S/\varphi = \pi$.

In Fig.7b the pure dephasing times of the tunable flux qubit are shown for different values of d. As expected, the coherence time increases when d increases. For $d = 0.75$ the typical Echo decay is expected to be about $2\mu s$ which is close to the best coherence times measured on flux qubits without SQUIDs [1].

3 Design and Fabrication

3.1 Design of the microwave resonator

The design of the microwave resonator, used to measure the qubit, is shown In Fig.8a. This coplanar waveguide resonator is fabricated by evaporation of a thin layer of superconducting aluminum (typically 150nm) on a sapphire wafer. Its designed parameters were chosen to be: f_r =11.6 GHz, $Z_0 = 50\,\Omega$ and $Q \sim 3000$.

Resonator Frequency

The coplanar waveguide geometry consists of a central conductor with ground planes on both sides. The effective dielectric constant felt by an electromagnetic field in this waveguide is given by [44] $\varepsilon_r = (1+\varepsilon_{r_{sap}})/2$ where $\varepsilon_{r,Sap} \approx 10$[3] is the dielectric constant of the sapphire wafer. As a consequence, the light velocity in the waveguide is $\widetilde{c} = c/\sqrt{\varepsilon_r} \approx 1.278 \cdot 10^8$ m/sec

The resonator - defined as a $\lambda/2$ segment of a transmission line- is terminated at both ends by capacitors that act as open circuit terminations. The frequency of the first mode is given by: $f_r = \widetilde{c}/2L$. Therefore, in order to have f_r =11.6 GHz, the length of the transmission line is $L = 5.5$mm.

Characteristic Impedance of the Resonator

The characteristic impedance of the coplanar waveguide was chosen to be matched to the impedance of the incoming coax $Z_0 = 50\Omega$. To achieve this, we defined its geometry such that $w_{tras} = 11/5 d_{tg}$ [44] where w_{tras} is the width of the central conductor and d_{tg} is the gap between the central conductor and the ground planes. In our current design, the width of the central conductor was chosen to be 11 μm and the gap d_{tg} was 5 μm.

Quality Factor of the Resonator

The quality factor of the resonator is fixed by the transmission coefficient of its open circuit terminations and therefore by the value of the coupling capacitor C_c represented In Fig.8a.

The reflection of an incoming wave is determined by the impedance mismatch and given by:

$$r_{L/R} = \frac{Z_0 - \left(Z_0 + \frac{1}{j\omega_r c_c}\right)}{Z_0 + \left(Z_0 + \frac{1}{j\omega_r c_c}\right)} = \frac{1}{2jC_c\omega_r Z_0 + 1} \tag{36}$$

Since our resonator has a high quality factor, the transmission coefficient $T_{L/R} = 1 - \left|r_{L/R}\right|^2 \ll 1$ is:

$$T_{L/R} = 1 - \frac{1}{1 + 4C_c^2\omega^2 Z_0^2} \sim 4C_c^2\omega_r^2 Z_0^2 \tag{37}$$

The quality factor due to the capacitor on the left (resp. right) side is given by $Q_{L/R} = \frac{2\pi f_r}{f_r T_{L/R}}$,where $\kappa_{L/R}$ represents the loss rate of the system on the left (resp. right) open termination. Therefore, the total quality factor of the system is given by:

$$\frac{1}{Q} = \frac{1}{Q_L} + \frac{1}{Q_R}$$

We decided to have the same loss rates on both sides of the resonator and therefore

$$Q = \frac{\pi}{4C_c^2\omega_r^2 Z_0^2}$$

The design parameter of the quality factor of the resonator is chosen to be $Q = 3000$, therefore we obtain a coupling capacitor C_c:

[3] Sapphire is a uniaxial substance with $\varepsilon_{r_{sap},z} = 11.5$ and $\varepsilon_{r_{sap},x-y} = 9.3$ where $\varepsilon_{r_{sqp}} \approx \left(\varepsilon_{r_{sap},z} + 2\varepsilon_{r_{sap},x-y}\right)/3 \approx 10.03$

$$C_c = \sqrt{\frac{\pi}{4Q}} \frac{1}{\omega_r Z_0} \approx 4.325\text{fF}$$

The dimensions of the coupling capacitor have been calculated with an electromagnetic simulator (Sonnet). We found that two pads of 50 μm width separated by a 5 μm gap will give us the correct capacitance value.

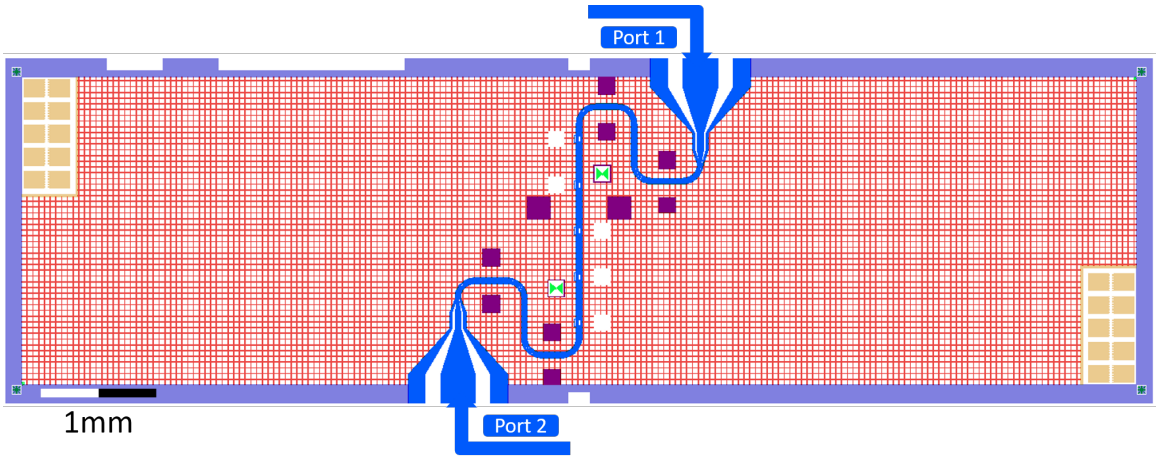

(a)

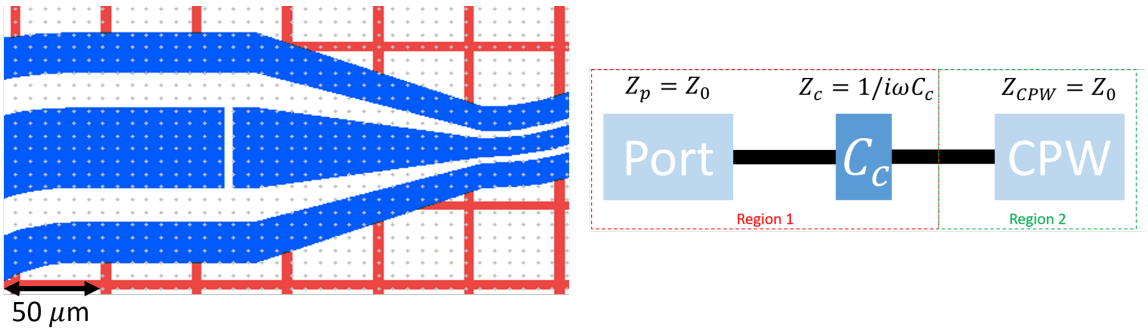

(b)

Figure 8: **(a)** Design of the resonator. **(b)** Zoom on the flux lines (in left) and on the coupling capacitor and an illustration of the impedance of the components on the left side of the resonator in the vicinity of the coupling point.

3.2 Design of the tunable flux qubit

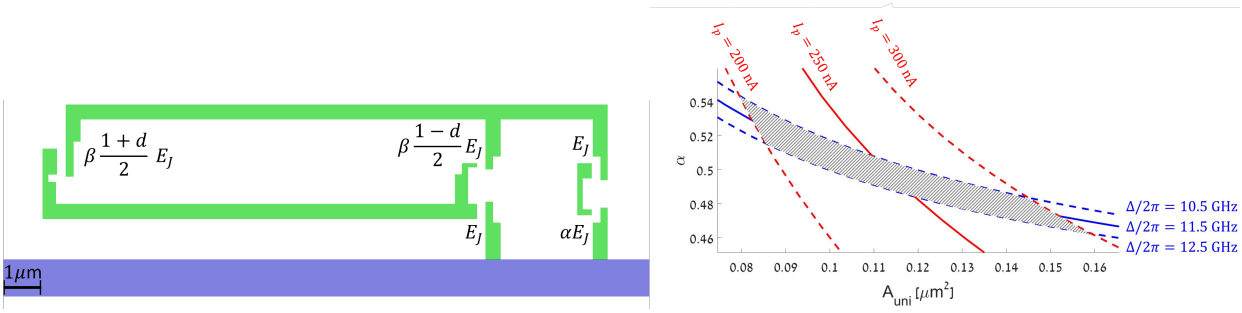

(a) (b)

Figure 9: **(a)** Design of the tunable flux qubit mask. The left loop is the SQUID, while the qubit area consists of the area of the two loops. The width of the wires of the qubit was taken to be 400nm. In this design, we present all the junctions as a function of the Josephson energy of the unitary junction E_J. The surface area of the unitary junction is $A_{uni} = 0.1145\mu\text{m}^2$, the small junction α was chosen to be $\alpha = 0.495$. The junctions of the SQUID have additional parameters, β and d. $\beta = 2$ is the multiplayer of the effective junction of the qubit and $d = 0.75$ it the asymmetry parameter of the squid. **(b)** Iso-Δ and Iso-I_P curves for $\Delta = 11.5 \pm 1\,\text{GHz}$ and $I_p = 250 \pm 50\,\text{nA}$.

Our qubit design, shown In Fig.9a, consists of two loops. The outer loop is the qubit's loop and it is galvanically connected to the resonator in order to increase the coupling (in the range of $\sim$ 100MHz). The left inner loop is the SQUID's loop. The areas of the qubit/SQUID loops are chosen such that $S_{qubit} = 3/2 S_{squid}$. Hence, when the flux qubit is tuned at the vicinity of one of its optimal points $\Phi/\varphi_0 = (2n+1)\pi$, the flux Φ_S inside the SQUID is given by:

$$\Phi_S/\varphi_0 = (2n+1)\pi\frac{S_{squid}}{S_{qubit}} = (2n+1)\times 2\pi/3 \tag{38}$$

The parameters of the flux qubit (Δ, I_p) are controlled by the parameters of the junctions (E_J, E_C, α) intersecting its loop. For a given oxidation, the values E_J, E_C depend only on the surface areas of the junctions A. Namely, $E_J \propto A$ and $E_C \propto 1/A$. Therefore, their product is a constant and depends only on the parameters of the dynamical oxidation recipe. The square root of this product defines what is called the **plasma frequency** of the junction. Using our standard evaporation recipe, this value is $f_{plasma} = \sqrt{8E_J \times E_C}/h \approx 87.71\,[\text{GHz}]$.

In our qubit design, we control the Josephson energy E_J and the capacitive energy E_C of the unitary junctions by changing the surface area of the junctions. In Fig.9b, we represent the parameters of the flux qubits as a function of S and α. In order to get a flux qubit with $\Delta \sim 11.5 + 1$GHz and $I_p \sim 250 \pm 50$ nA, we see clearly that the surfaces of the unitary junction should be $A_{uni} \sim 0.11 \pm 0.04\mu\text{m}^2$ and $\alpha = 0.495 \pm 0.04$.

3.3 Fabrication Process Recipe

In the following we will present our fabrication process in a table, step by step.

Parameters of the sample:

Our sapphire wafer is 2-inch wafer and 330μm thin from Crystec. It is cut at the a-plane of the crystal and double-sided epipolished. For convenience, we cut the wafer into rectangular coupons, each one containing 10 samples.

Name	Shape	height	length
sapphire wafer	circular	2 inch	2 inch
coupon	rectangular	21 mm	23.1 mm
sample	rectangular	3 mm	10 mm

Dicing - cut the wafer to coupons

It is more convenient to process square coupons than a full wafer. Therefore, we dice our wafer into coupons before process according to the following recipe:

Step #	Process Name	About the process
1	Spin Coating	E-Beam-resist *EL7*. 500 rpm 2s, 2000 rpm 60s
		Hot plate, 120°C, 1 minute
		E-Beam-resist *EL7*. 500 rpm 2s, 2000 rpm 60s
		Hot plate, 120°C, 1 minute
		E-Beam-resist *EL7*. 500 rpm 2s, 2000 rpm 60s
		Hot plate, 120°C, 5 minutes
2	Dicing	Front dicing in three steps: Every step remove 140μm of sapphire
3	Cleaning	IPA, to remove the plastic cover from the samples
		Stream of acetone to remove big particles
		NMP over night 90°, Water, IPA, $N2$ Blow Dry

* Note, the width of the dicing saw in the our machine has 300μm width. The average width of the diced canal is roughly 350μm. Therefore, the space between the resonators cannot be smaller than 400μm.

Alignment marks

For E-beam lithography, alignment marks are needed to align the qubits with the resonators. Niobium marks are much more visible than the ones made out of aluminum. This process is done only once for each coupon. Indeed, niobium is resistant to the Piranha acid cleaning.

Step #	Process Name	About the process
1	Cleaning	Piranha acid 10min, water, IPA, N_2 Blow-dry
2	Heating	Hot plate, 180°C, $10-15$ minutes (Inside the clean room)
3	Evaporation	150 nm Aluminum layer evaporation
4	Heating	Hot plate, 180°C, 2 minutes
5	Spinning resist	E-Beam-resist *EL7*. 500 rpm 2s, 2000 rpm 60s, 6000 rpm 2s
6		Hot plate, 180°C, 1 minute
7		E-Beam-resist *EL7*. 500 rpm 2s, 2000 rpm 60s, 6000 rpm 2s
8	Pre-bake	Hot plate, 180°C, 15 minutes
9	Evaporation	60 nm Germanium layer evaporation
10	Spinning resist	E-Beam resist *CSAR*. 500 rpm 2s, 4000 rpm 60s, 6000 rpm 2s
11	Pre-bake	Hot plate, 100°C, 5 minutes
		Crestec 9000, 30pA, $Dose = 666uC/cm^2$
12	Development	*MIBK* - 4min, *IPA* - 1min
11	Etching	$7-10$ minuets with stirrer Al etch until homogeneous with eye + 20% waiting
		1 min AZ726, Water
12	Evaporation	100 nm Niobium layer evaporation
13	Lift off	NMP 90° until the Niobium layer is removed
14	Cleaning	Piranha acid 10min, water, IPA, N_2 Blow-dry

* Note, step 14 is recommended but not mandatory.

UV Lithography

In this step, we fabricate the coplanar waveguide resonator. The fabrication of the resonator is done by evaporating a single layer of 150nm on the full sapphire coupon. After this, we etch this aluminum using Al-etchant according to our photoresist mask.

Step #	Process Name	About the process
1	Cleaning	Piranha acid 10min,water, IPA, N_2 Blow-dry
2	Heating	Hot plate, 180°C, $10-15$ minutes (Inside the clean room)
3	Evaporation	150 nm Aluminum layer evaporation
4	Heating	Hot plate, 180°C, 2 minutes
5	Spinning resist	Photo-resist $AZ1505$. 500 rpm 2s, 5000 rpm 60s, 6000 rpm 2s
6	Pre-bake	Hot plate, $80°C$, 5 minutes
7	UV lithography	$MLA\,150$, $Dose = 23$ [mJ/cm^2], CD(x,y) $-600, -600$
8	Development	AZ726 45s, Water 45s, N_2 Blow Dry 45s
9	Post Bake	Hot plate, 120°C, 5 minutes
10	Residual removal	$O_2 + N_2$ ashing 50% 1 minute
11	Etching	$7-10$ minuets with stirrer Al etch until homogeneous with eye + 20% waiting
		1 min AZ726, Water
12	Cleaning	NMP over night, Water
		Sonication 80KHz, 50%, $50C°$ - Acetone 30sec, IPA 30sec, N_2 Blow Dry 45s

E-Beam Lithography

The fabrication of the qubits is made by ebeam lithography and with the so-called double evaporation technique. Two thin layers of superconducting aluminum are evaporated through a germanium mask created by Ebeam lithography/RIE technique. Before the evaporation, an ion milling step removes the oxide layer from the central conductor of the resonator[4] in order to establish a good electric contact. A first layer of 20nm Al is evaporated in a direction of $-25°$ relative to the sample axis. Then, a dynamical oxidation of the Al layer is done by introducing a flow of O2/N2 in the sample chamber (typ. P~19ubar). This step is followed by a second evaporation of a 30nm Al layer in the opposite direction with an angle of $+25°$.

Step #	Process Name	About the process
1	Heating	Hot plate, 180°C, 5 minutes
2	Spinning resist	E-Beam-resist $EL7$. 500 rpm 2s, 2000 rpm 60s, 6000 rpm 2s
		Hot plate, 180°C, 1 minute
		E-Beam-resist $EL7$. 500 rpm 2s, 2000 rpm 60s, 6000 rpm 2s
3	Pre-bake	Hot plate, $180°C$, 15 minutes
4	Evaporation	60 nm Germanium layer evaporation
5	Spinning resist	E-Beam resist $CSAR$. 500 rpm 2s, 4000 rpm 60s, 6000 rpm 2s
6	Pre-bake	Hot plate, $100°C$, 5 minutes
7	E-Beam lithography	*Crestec 9000*, $30pA$, $Dose = 666uC/cm^2$
8	Development	$MIBK$ - 4min, IPA - 1min

* You should do steps 1-3 with an additional dummy sample that will be used as a reference for the Germanium etch during the RIE process.

[4] Only on specific location where the constriction are connecting to the resonator

RIE and Cold Evaporation

Step #	Process Name	About the process
1	location	Locate the real and dummy sample in the middle of the wafer
		Be sure that the samples are laying next to the other
		Be sure that the samples are well pressed to the wafer
2	Calibration	Set the software to interferometer mode
		Focus the laser beam on the dummy wafer
3	Etching	Choose FS6 slow etch
		Count the time takes the sinusoidal shape to top
		Wait more 80% of the time (180% of the time in total)
5	Residual removal	$O_2 + N_2$ ashing 50% 8 minutes
6	Cold Evaporation	20nm layer at -44°C
		dynamic oxidation $-10° - +4$°C at pressure of 0.019mbar
		Second layer $4° - 10$°C
		Static oxidation for 10min
7	Cleaning	NMP over night, Water, IPA, $N2$ Blow Dry

Dicing - cut the coupons to samples

As mentionned earlier, each coupon constains ten samples (10×3mm each). Therefore, we should now cut the coupon into ten samples. During this process, we measured that the resistance of the junctions is increased by $\sim 12\%$.

Step #	Process Name	About the process
1	Spin Coating	E-Beam-resist $EL7$. 500 rpm 2s, 2000 rpm 60s
		Hot plate, 120°C, 1 minute
		E-Beam-resist $EL7$. 500 rpm 2s, 2000 rpm 60s
		Hot plate, 120°C, 1 minute
		E-Beam-resist $EL7$. 500 rpm 2s, 2000 rpm 60s
		Hot plate, 120°C, 5 minutes
2	Dicing	Front dicing in three steps: Every step remove 140μm of sapphire
3	Cleaning	IPA , to remove the plastic cover from the samples
		Stream of acetone to remove big particles
		NMP over night 90°, Water, IPA, $N2$ Blow Dry

* Note, the width of the dicing saw in the our machine has 300μm width. The average width of the diced canal is roughly 350μm. Therefore, the space between the resonators cannot be smaller than 400μm.

3.4 Room temperature characterization

At the end of the fabrication process we observe our sample by an optical microscope and by an Atomic Force Microscope (AFM). The optical microscope has low resolution but allows us checking the sample for unwanted shorts between elements and resist particles that we could not get removed. The AFM scan has an ultra-high resolution and allows us to extract critical information concerning the RIE and the Ebeam step: i.e. qualitative shape of the qubit, dimensions of the junctions, surface roughness of the wafer, remaining particles of resist...

In Fig.10.a, we present a microscope picture of one sample. As explained in Sec.1.4, our resonator is a superconducting coplanar waveguide made of 150nm thick of evaporated aluminum on a Sapphire wafer connected to a cryogenic PCB connector. The resonator consists of three islands. The right and the left are grounded and connected via an air bond in the middle of the sample. The third island is the central conductor. It crosses the sample at the center and acts as a transmission line. The resonator parameters are as explained in Sec.3.1 $w = 11\mu$m and $d = 5\mu$m, such that the characteristic impedance is $Z_0 \approx 50\Omega$.

In figure 10.b, we present an AFM micrograph of a one of the fabricated tunable flux qubits. The qubit and the resonator (green) are galvanically connected to increase the coupling between them. These two elements were fabricated together by using a double-angle evaporation technique as described in Sec.3.3.

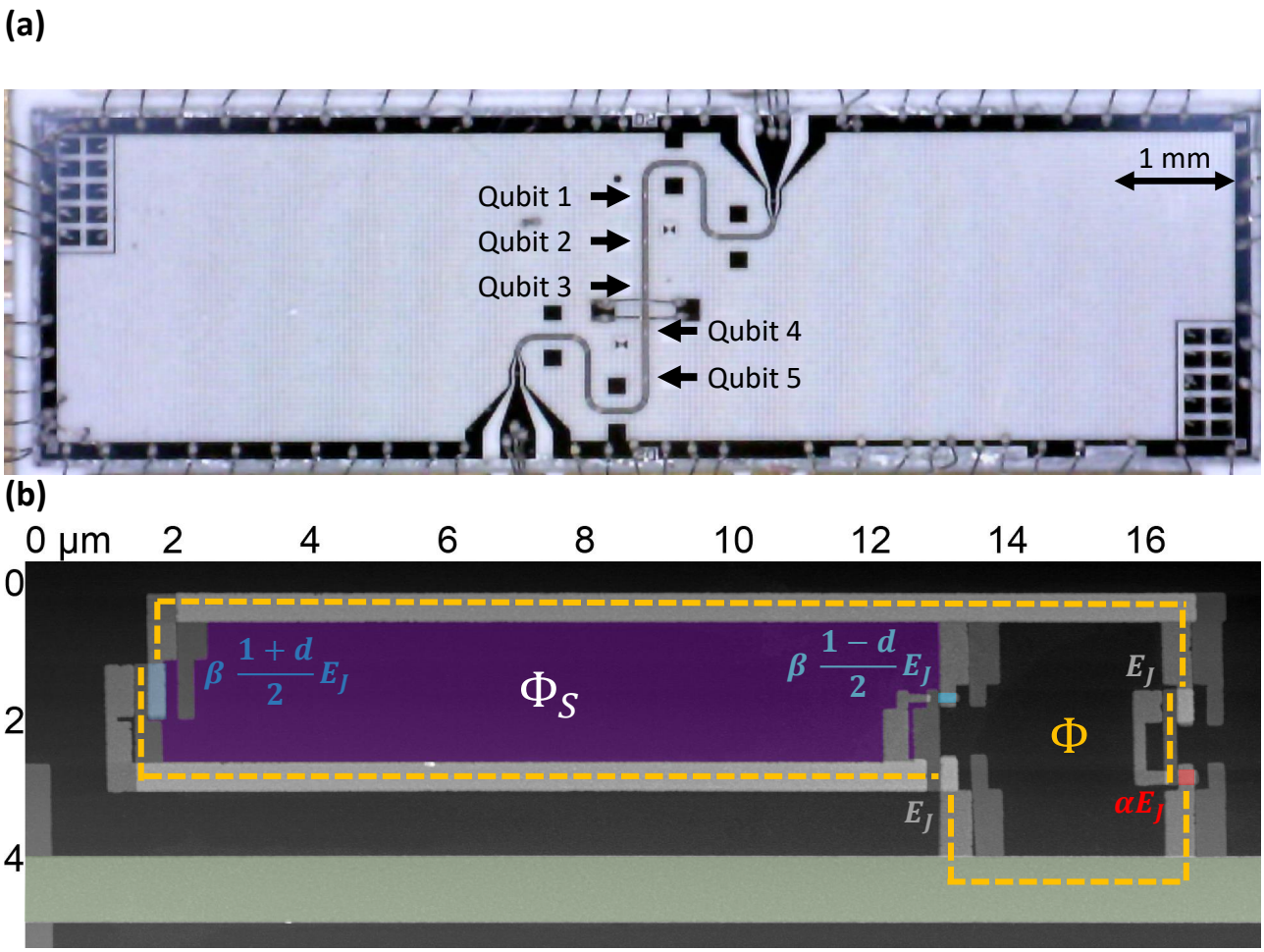

Figure 10: **(a)** Microscope picture of the whole sample, showing the coplanar waveguide resonator inductively coupled to five tunable flux qubits. The resonator is made of 150nm thick evaporated aluminum on a sapphire wafer laid on a PCB layer. The right and left aluminum grid are grounded and connected via an air bond. The pads in the top left and bottom corners right are dedicated to test junctions. **(b)** AFM micrograph of a tunable flux qubit. The qubit is galvanically coupled to the central conductor of the resonator (green line). It consists of two loops sharing one Josephson junction. The Outer loop (yellow) is the qubit loop, having an area of $S_{right} = 43.71\mu\text{m}^2$. This loop is is intersected by three Josephson junctions. Two of them are unitary Junctions having a surface area of $A_{uni} \approx 0.104\,\mu m^2 \pm 7.6\%$ and one that has a Josephson energy of αE_J having a surface area of $A_\alpha \approx 0.0465\,\mu\text{m}^2 \pm 9.9\%$. The qubits loop is also intersected by a SQUID loop (purple), having an area of $S_{squid} = 29.72\,\mu\text{m}^2$. The SQUID is intersected by two Josephson junctions with surface areas are $A_{big} \approx 0.192\mu\text{m}^2 \pm 6.4\%$ and $A_{small} \approx 0.0338\,\mu\text{m}^2 \pm 12\%$ for the big (dark blue) and the small (bright blue) junctions, respectively. The area inside the yellow dashed line is the total area of the tunable flux qubit.

The outer loop (yellow) is intersected by two unitary junctions (gray) having an area of $A_{uni} \approx 0.104\mu\text{m}^2 \pm 7.6\%$. The smaller junction α-junction (red) having an an area of $A_\alpha \approx 0.0465\mu\text{m}^2 \pm 9.9\%$, which corresponds to $\alpha = 0.45 \pm 0.06$. In addition, the outer loop is also intersected by a big junction that also intersects the SQUID's loop. It is the biggest junction having a surface area of $A_{big} \approx 0.192\mu\text{m}^2 \pm 6.4\%$ while the second junction of the SQUIDs loop is the smallest junction of the qubit having a surface area of $A_{small} \approx 0.0338\,\mu\text{m}^2 \pm 12\%$ such that $d \sim 0.7 \pm 0.03$ and $\beta \sim 2.17 \pm 0.26$.

At the limit where $d \to 1$, most of the current, I_p, will flow through the big junction. Therefore, the qubit's effective junction will be determined by the position of this junction, inner or outer line. In our qubit,

the asymmetry of the SQUID was chosen to be high $d \sim 0.7$, and the big junction was located on the outer loop. Therefore, the effective area of the qubit is in a good approximation the area of the outer loop.

As mentioned earlier, the area of the SQUID was chosen to be roughly two-thirds of the area size of the qubit loop. We measure $S_{SQUID} = 29.72\mu m^2$ and $S_{qubit} = 43.71\mu m^2$ and find that the ratio $S_{squid}/S_{qubit} \sim 0.68$ in agreement with our design.

IV characterization of junctions

The IV characteristic of the test junctions is the second measurement we perform before putting the sample into the dilution fridge. The test junctions are fabricated with the qubits simultaneously. Therefore, one can assume that the resistance of these junctions would be similar to the ones of the qubit. The junction's resistance is related to its Josephson energy E_J by the Ambegaokar-Baratoff relation [45] to the critical current crossing the junction at 4K temperature.

$$I_0 R(T = 4\text{K}) = \frac{\pi \Delta_g}{2e} \approx 330\mu\text{V}$$

where $\Delta_g \approx 210\mu$eV is the superconducting gap of a thin layer of aluminum as evaluated from Fig.11 taken from [46].

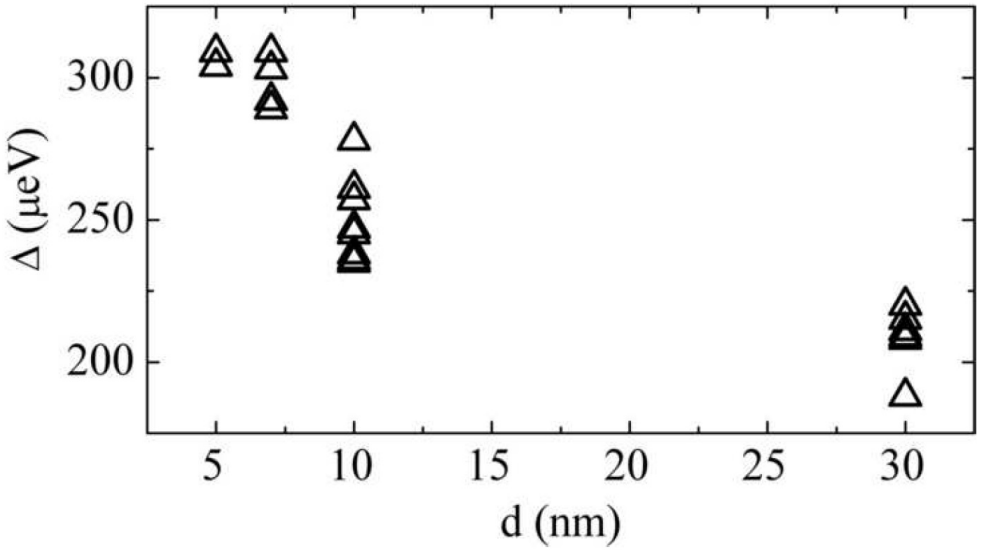

Figure 11: Taken from [46] Observed superconducting energy gap of aluminum as a function of film thickness. Each point represents a single junction whose gap energy was extracted via differential conductance measurements. Films were evaporated onto a substrate in contact with a liquid nitrogen cooled stage at a temperature of $\sim$ 173K.

The temperature dependence of the resistance is such that $R(T = 300\text{K}) = 1.15 \cdot R(T = 4\text{K})$, therefore:

$$\boxed{I_0 R(T = 300\text{K}) = 286\mu V}$$

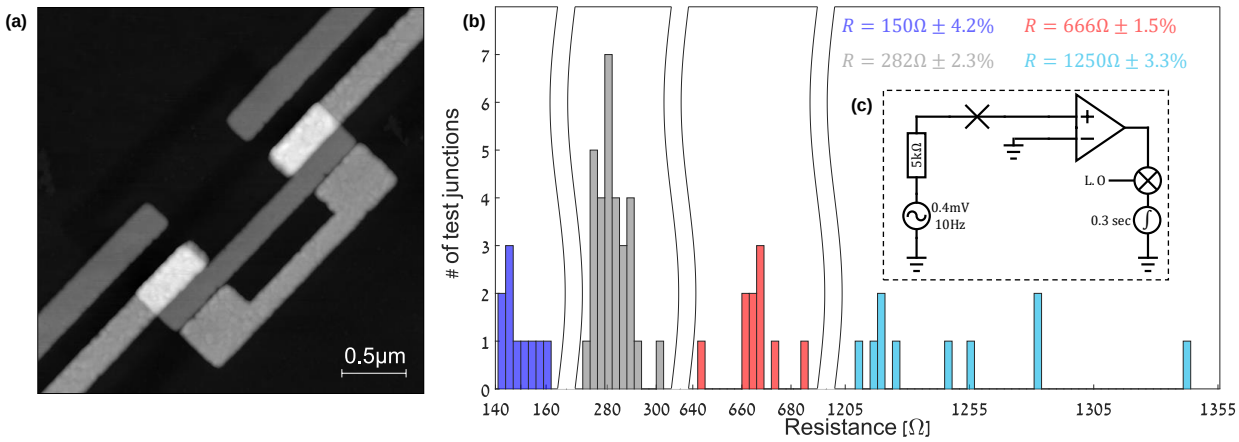

Figure 12: **(a)** An AFM micrograph of one of the unitary test junctions. **(b)** A histogram consists of bins with a 3 Ohms width, representing the resistance distribution of 60 test junctions: 30 unitaries (gray), ten αs (red), ten $\beta\frac{1+d}{2}$ (dark blue), and ten$\beta\frac{1-d}{2}$ (bright blue). The variation of the resistance shrinks while the size of the junction increases. from the resistance of the qubit can give a good approximation for the Josephson energy can be found from the expression $E_J = \varphi_0 \cdot \Delta_g / R$ where $\Delta_g = 210\mu$eV is the superconducting gap of aluminum. **(c)** A sachem of the measurement setup. The diagram was drawn by using https://www.circuit-diagram.org web site.

The IV measurements have been performed using a probe station in a so-called two probe measurement. The probe station is connected to a lock-in amplifier having an internal A.C. voltage source (local oscillator - LO). The voltage getting out from the source is a sine wave. Its amplitude is 4mV, and it oscillates at 10Hz frequency, as shown in Fig.12.c. The current passing through the junction is measured by the lock-in amplifier by mixing it with the local oscillator, and integrating over 300ms. The integration process suppresses noise and out-of-phase signals due to the orthogonality of the sine functions.

In Fig.12.b, we present a histogram showing the resistance distribution of the test junctions. Each bin in the histogram represents a 3Ω width, and its height represents the number of junctions inside this range.

The statistics of the test junctions presented in Fig.12.b were taken from 60 test junctions where half of them are the unitary junction (gray), and the rest alpha (red) , $\beta\frac{1+d}{2}$ (dark blue), and $\beta\frac{1-d}{2}$ (bright blue) junctions are equally divided, ten each. We get deviations of the resistances in the range of $1.5\% - 4.2\%$. Using these measurements, we can extract the parameters of the qubit: $\alpha = 0.42 \pm 0.01$, $d = 0.79 \pm 0.01$ and $\beta = 2.11 \pm 0.09$.

This measurement in association with AFM scan, Fig.12.a, enables us to extract the resistance $R_{ns}(T = 300\text{K}) = R_{jun} * S_{Jun}\,[\Omega.\mu\text{m}^2] = 35[\Omega.\mu\text{m}^2]$.

4 Experimental Setup

The sample is glued to a PCB holder , which is embedded in an OHFC copper box. This box is placed inside a superconducting coil in the 20mK stage of a dilution fridge. In order to protect the qubits from Earth's magnetic field fluctuations, the superconducting coil is placed inside two protecting shields. An external copper box covered with $10 - 15$ μm of SnPb 60/40 acts as a superconducting shield. In addition, this copper box is surrounded by a CryoPerm (mu-metal) 1 mm thick shield. The coil is connected to superconducting twisted wires up to a Fisher 2pin shielded connector located at the 5K stage and then to Phosphore bronze (AWG 27) twisted wires from 5K to 300K. Outside the fridge, a low pass filter is made out of a a 5KΩ resistor placed in well-controlled temperature environment and connected to capacitors (see.5). This filter is connected to a low-noise DC power supply [47] with noise power spectrum of $15\text{nV}/\sqrt{\text{Hz}}$ at 10KHz (generating $0.1\mu\Phi_0/\sqrt{\text{Hz}}$ of magnetic flux noise).

In order to probe the qubit, we use an OPX system from Quantum Machines. The OPX has two outputs that can generate pulses modulated with an intermediate frequency (IF) $f_{int} \leq 250$MHz. In each port, the IF signal is mixed by an IQ modulator with a microwave LO signal coming from a Keysight microwave generator [48], as shown in Fig.13. The amplitude of the RF signal is controlled by a fast ramping switch [49]

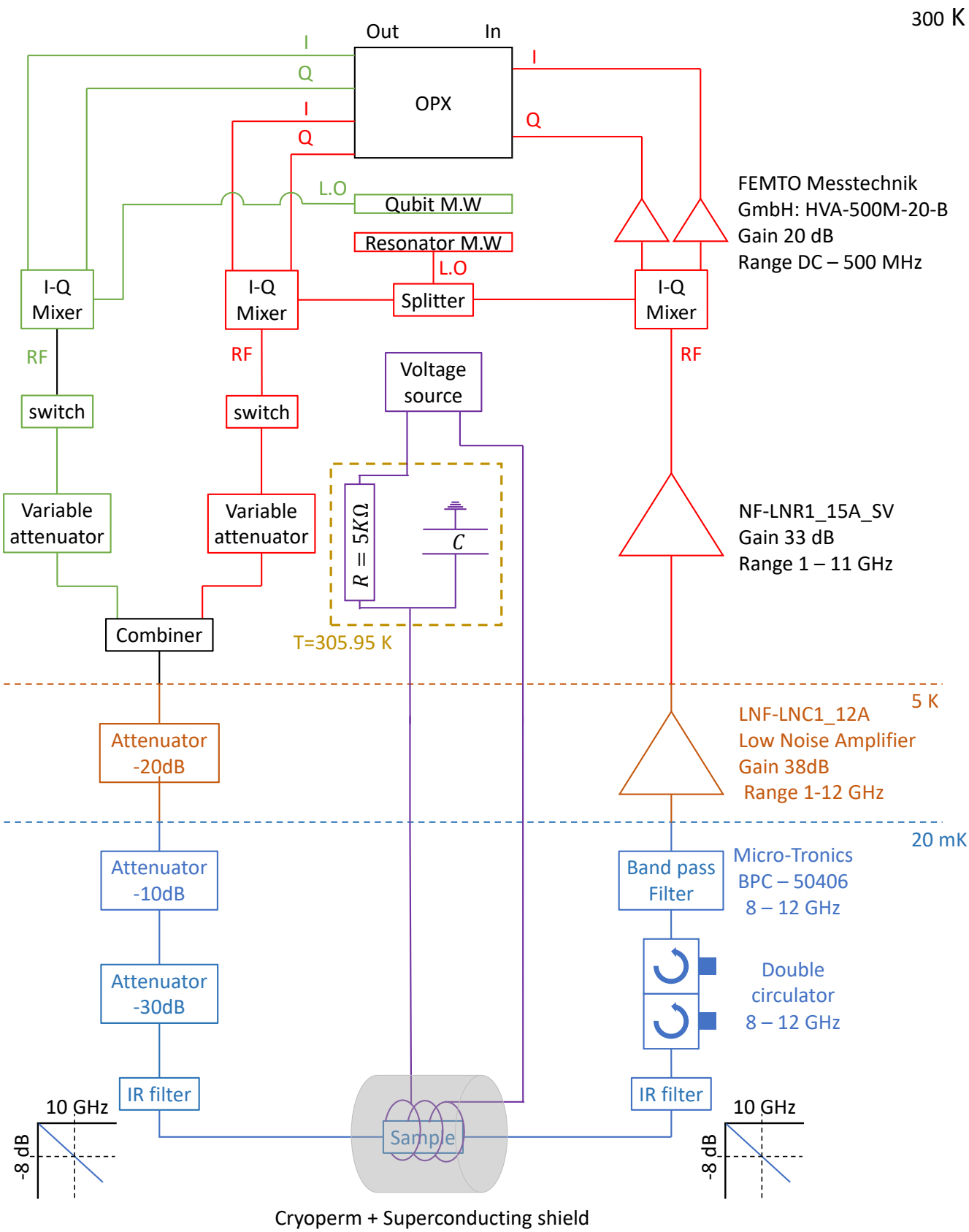

Figure 13: A scheme of the experimental setup.

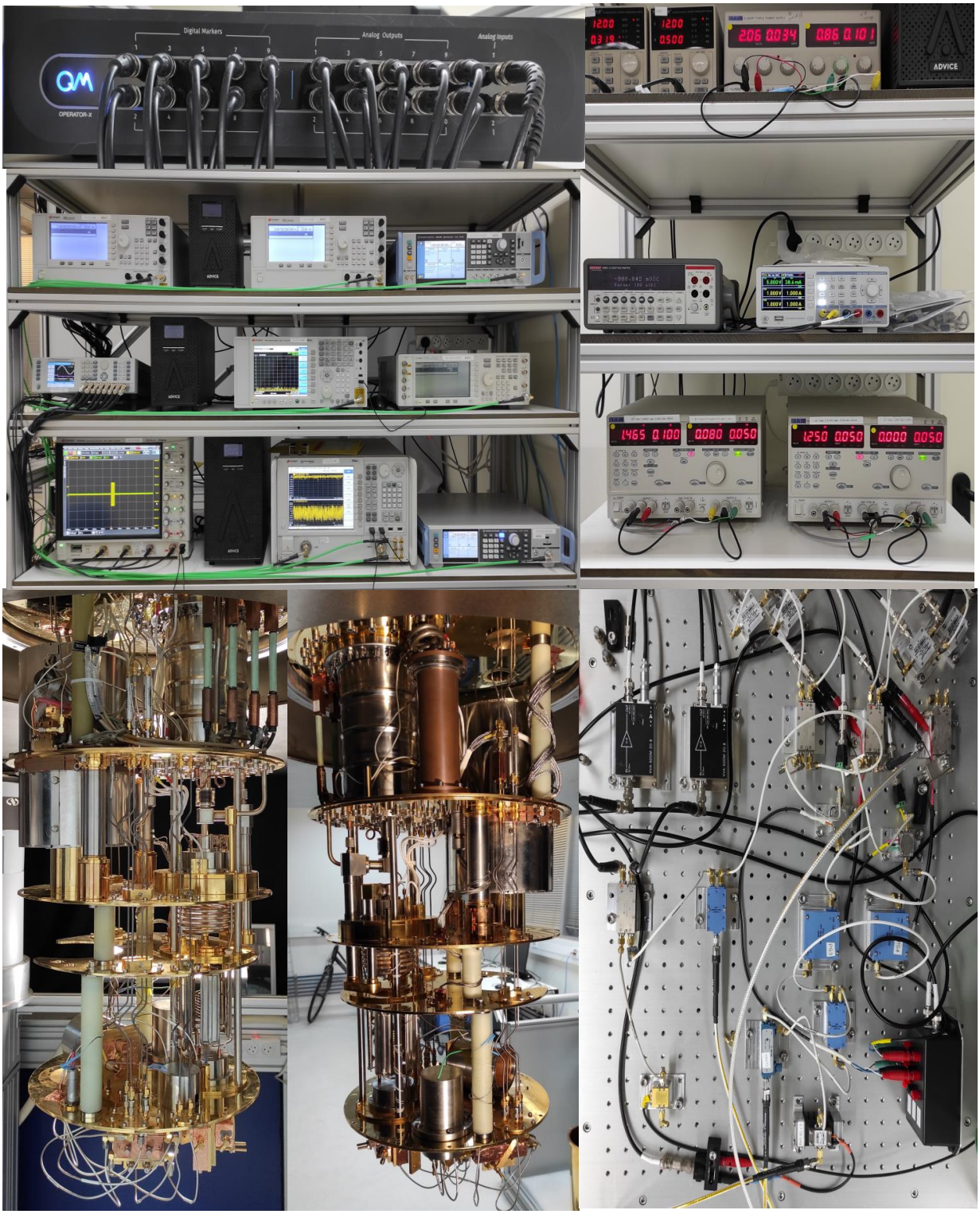

Figure 14: Pictures of the system

(~30ns rise time) and a variable attenuator [50]. The noise temperature of these signals is about 300K. The number of incoming thermal photons is given by the Bose-Einstein distribution:

$$\bar{n} = \frac{1}{\exp(\frac{hf}{K_B T}) - 1} \tag{39}$$

where T[K] is the temperature, K_B is the Boltzmann constant, and f is the frequency [Hz]. At 300 K and $f_{res} = 10$GHz, $\bar{n}_{300} \sim 600$.

A first attenuator of -20dB, located at the 5K stage of the fridge decreases this number by a factor 100. The number of incoming photons is thus reduced to $\bar{n}_{tot,5\text{K}} = n_{300\text{K}}/100 + \bar{n}_{5\text{K}} \sim 16.13$ photons, where $\bar{n}_{5\text{K}}$ is the number of thermal photons generated by the attenuator thermalized at 5K. At the entrance of the 20mK stage, there is a second attenuator of -40dB that lowers this number to $16 \cdot 10^{-4}$ photons. The number of photons that are thermally generated at 20mK is extremely low $\sim 3.5 \cdot 10^{-11}$.

At the output of the resonator, we cannot use attenuators in order to prevent incoming thermal noise. Therefore, we use a double circulator that passes the signal from the resonator but blocks by ~ -40 dB incoming thermal noise from the amplifier.

The first HEMT amplifier is located at the 5K stage of the fridge. It has a gain of 38dB at the frequency $f_r = 10$GHz and a noise temperature of 5K. Consequently, we are limited by the thermal noise that is coming from the environment with effective cavity temperature $T_{cav} = 80$mK. The signal to noise ratio ($SNR = \frac{P_{meas}}{P_{noise}}$) of our measurement is fixed by the ratio of the input power P_{in} at the exit of the resonator with the Johnson noise power $P_{noise} = 4K_B T \Delta f$ [51] where K_B is the Boltzmann constant, Δf is the bandwidth in Hz and $T = 10$K is the sum of the stage and the noise temperatures of the amplifier. Hence, the bandwidth required to perform a measurement with $SNR = 1$ and with a single photon in the resonator ($\bar{n} \approx 2Q_c/\hbar\omega_r^2 \times P_{meas} = 1$ [25]) is $\Delta f \sim 100$KHz.

Outside the fridge, the signal is amplified again by 33dB. Then it passes through the $I-Q$ demodulator. Then the signals I and Q are amplified by 20dB, each, using FEMTO amplifiers [52] and is digitized and demodulated (at the intermediate frequency) by the OPX.

5 Results

5.1 Anticrossing Scan:

The measurement of the resonator transmission is done by a Keysight PNL Vector Network Analyzer (VNA) when the current flowing in the coil is zero. In Fig15.b we present the VNA scan (blue) and its fit with a lorentzian behavior (orange) (see Eqn.24). We obtain $\omega_r/2\pi = 10.2246$GHz, $Q_{tot} = 3560$ in agreement with the design parameters.

In a second step, we sweep the current flowing through the coil. When the magnetic flux generated by the coil is at the vicinity of the optimal point of one of the qubits, the resonance frequency of the resonator ω_r will shift upwards (resp. downwards) when the qubit gap Δ is lower (resp. higher) than ω_r. When Δ is lower than ω_r we observe an anticrossing pattern and the resonance frequency $\omega_{r,shift}$ will reach $\omega_r \mp 2g$. This allows us to measure precisely the value of the coupling constant g for each qubit.

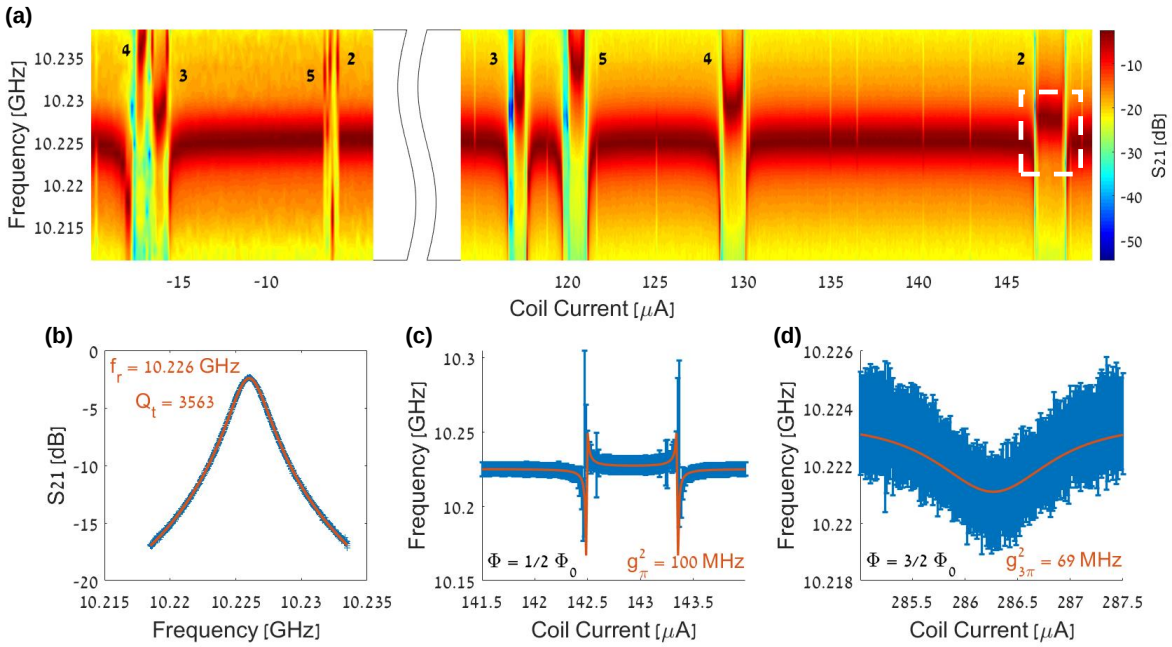

Figure 15: **(a)** A 2D figure of S_{21} as a function of coil current and resonator frequency for two different coil current regimes that are translated into magnetic fluxes of $\Phi/\varphi_0 = -\pi$ and $\Phi/\varphi_0 = \pi$ (left and right respectively) for different qubits. The resonator's resonance frequency remains constant while the current in the coil is changing till the generated magnetic flux falls in the vicinity of the optimal point of one of the qubits, then the resonance frequency will shift. The direction of the resonance frequency shift is controlled by the detuning of the frequency gap of the qubit Δ from the resonance frequency ω_r, $\Delta_R = \omega_r - \Delta$. For positive values, an anticrossing appears, and for negative, a deep appears. Here we get four distinguished anticrossings that are associated with the qubits as appear on the graph. **(b)** Scan of the resonance frequency (blue) and fitted function (orange). **(c-d)** Zoom around the anticrossing (c) and the deep (d) regions of qubit 2. The blue carves are the error bars, and the oranges are the fits, which are obtained by fitting the coupling constant using the full Hamiltonian of the system.

In Fig.15.a, we present a $2D$ scan of the VNA scan as a function of the current flowing through the coil. For different qubits, the anticrossing appears at different values of magnetic fields due to magnetic field inhomogeneities and slight changes in the size of each qubit loop. This scan shows four qubits, where qubit one is too close to qubit three on the negative side and did not appear on the positive side during this scan.

In Fig.15.c and Fig.15.d, we present a close-up scan when the magnetic flux is near the optimal points $\Phi/\varphi_0 = \pi$ and $\Phi/\varphi_0 = 3\pi$ of qubit 2. In the first figure, an anticrossing is observed, which means that the $\Delta < \omega_r$. In the second figure, $\Delta > \omega_r$. In both figures, the blue lines are the error bars of fitted resonance frequency as fitted In Fig.15.a, and The orange line is obtained by diagonalizing the full Hamiltonian of the system and fitting the coupling parameter g. From this fit, we obtain the value of the coupling between the resonator and the qubit ($g = MI_p\delta I_0/\hbar$).

5.2 Qubit Spectroscopy

The qubit spectroscopy allows us to extract the parameters of each qubit Δ and I_P for different values of the flux Φ_S threading the SQUID. In order to detect the qubit, we sweep the pump frequency of a saturation pulse of 23 μs length and power of P_{pump} =-100dBm. When the pump frequency is in resonance with the qubit, this pulse puts the system into a statistical mixture such that the probability of measuring the qubit at excited or ground state is equal. Right after the pump, a measurement pulse of $\sim 4\mu$s length and tuned at frequency 10.2246GHz and power $P_{meas} = -133$dBm is sent in order to detect the state of the qubit according to the mechanism described in 1.4. For each point, the measurement sequence is repeated and averaged over 2500 times in order to obtain an SNR of 30dB.

In the following we will present a spectroscopy scan of qubit 4 while the flux threading its loop was at

the vicinity of $\Phi^3/\varphi_0 = \pi(2n+1)$, where $n \in \{-1, 0, 1, 2\}$

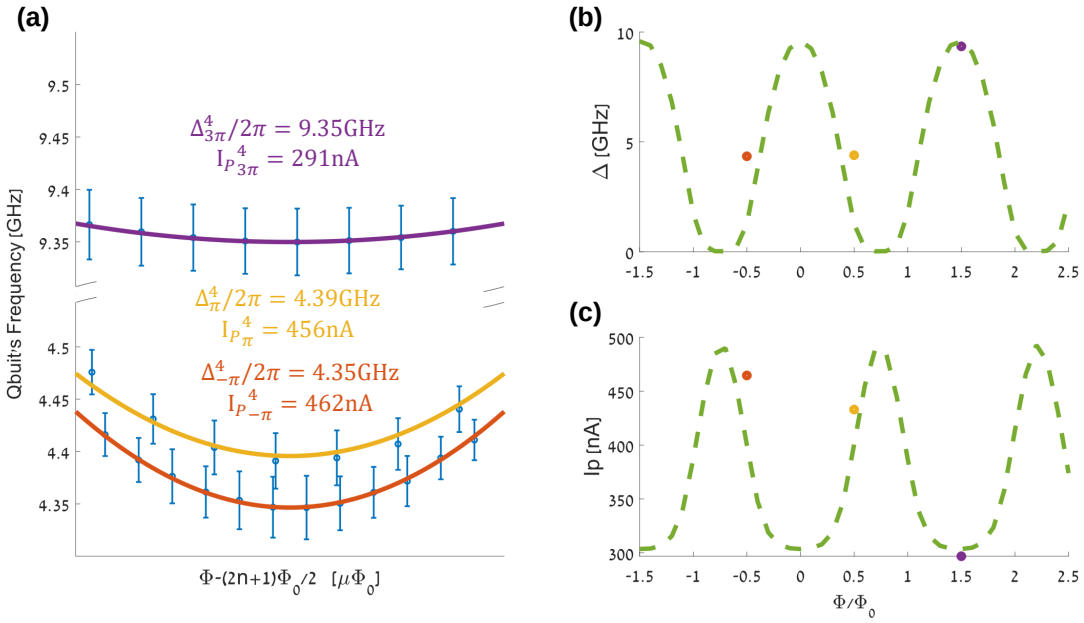

Figure 16: **(a)** Spectroscopy scan of qubit 4 in the vicinity of different optimal points. The red curve represents the measurement around $\Phi/\varphi_0 = -\pi$, the yellow is around $\Phi/\varphi_0 = \pi$ and the purple is around $\Phi/\varphi_0 = 3\pi$ **(b-c)** The qubit gap frequency Δ (b) and persistent current I_p (c) for different optimal points $\Phi^4/\varphi_0 = \pi(2n+1)$ where $n \in \{-1, 0, 1, 2\}$. The green dashed line is a fit with our model.

In Fig.16 we present a spectroscopy scan of qubit 4 around three different optimal points. The red and the yellow curves are the measurements around $\Phi^4/\varphi_0 = -\pi$ and $\Phi^4/\varphi_0 = \pi$, respectively, and the purple is around $\Phi^4/\varphi_0 = 3\pi$.

When $\Phi^4/\varphi_0 = 3\pi$, the flux threading the SQUID $\Phi_S/\varphi_0 \sim 2\pi$. It means that is effective energy of the SQUID becomes βE_J, and the qubit gets its non-tuned gap $\Delta^4_{3\pi} = \Delta^4_{real}$ and persistent current $I^4_{p,3\pi} = I^4_{p,real}$. For $n \neq 1$ the magnetic flux inside the SQUID is no longer an integer number of 2π, therefore the gap of the qubit decreases and the current increases.

In table 1 we present the measured values of the qubits gap Δ (top) and the persistent current I_p(bottom) of the qubits at each optimal point.

Magnetic flux	Qubit 1		Qubit 2		Qubit 3		Qubit 4		Qubit 5	
	Δ[GHz]	I_p[nA]	Δ[GHz]	I_p[nA]	Δ[GHz]	I_p[nA]	Δ[GHz]	I_p[nA]	Δ[GHz]	I_p[nA]
$-\Phi_0/2$	-	-	6.76	418	7.06	364	4.35	463	7.81	362
$\Phi_0/2$	7.12	380	6.88	369	6.77	366	4.39	456	7.88	362
$3\Phi_0/2$	12.26	245	12.41	239	12.62	244	9.35	291	13.5	232
$5\Phi_0/2$	8.00	323	7.04	318	8.25	357		-	9.61	287

Table 1: evaluated Δ and I_p of all the qubits presenting the tunability of the qubit as a function of the flux threading the qubit. We see that all the qubits has the same behavior in terms of Δ and I_p while the magnetic flux that threading the qubit changing.

From table 1, we get that all the qubits have qualitatively the same behavior. At $\Phi/\varphi_0 = 3\pi$, the gaps Δ of all the qubits is sensibly larger than at $\Phi/\varphi_0 = \pi$. This indicates that all the qubits are tunable. Yet, the tunability of the qubits seems bigger than what was predicted by the model described in Sec.2.2 We attribute this mismatch to the kinetic inductance of the SQUID loop, which was up to now neglected.

Kinetic inductance

In the model shown in Sec.2.1, we neglected the kinetic inductance of the SQUID L_k. But the SQUID, in our qubit, consists of long and thin wires such that L_k is not negligible in front of Josephson inductance $L_{J_{big}}$ of the big junction. Hence, the kinetic inductance should be added to the potential energy of the SQUID as will be shown below. The value of the kinetic inductance is given by:

$$L_K = \frac{R(T = 4\text{K})}{\pi \Omega_g}$$

where $\Omega_g = 320 \times 10^9\ rad\, s^{-1}$ is the angular frequency corresponding to the superconducting gap of a 25nm-thin film of aluminium and R_S is the resistance of the SQUID's loop. At $T = 4$K the resistance per square of aluminum is $R_\square = 3\Omega/\square$ [53]. The SQUID has a total number of 73 squares and therefore we can estimate its kinetic inductance to be $L_k \sim 0.22$nH.

In our model, we treat the SQUID loop and the big junction as an effective junction with an effective Josephson junction:

$$E_{J_{big-eff}}/h = \frac{\varphi_0^2}{L_{J_{big}} + L_{k_s}}/h = 387\text{GHz}$$

In figure 16.b-c we present the gap Δ (top) and the current I_P(bottom) as a function of the magnetic flux threading the qubit and compare it with our theory. Since all the qubits were fabricated together, we assume that $E_c = 0.96$GHz and $E_J = 660$GHz are the same for all the qubits. In table 2, we present the qubit fitted parameters. The average values of the qubit parameters are $\alpha = 0.37 \pm 0.01$, $d = 0.67 \pm 0.02$ in relative good quantitative agreement with our AFM and room temperature IV characterization 3.4.

	Qubit 1	Qubit 2	Qubit 3	Qubit 4	Qubit 5
α	0.375	0.362	0.37	0.397	0.357
β	2.1	2	2.13	2.16	2
d	0.68	0.68	0.7	0.64	0.65
L_k[nH]	0.44	0.45	0.45	0.45	0.45

Table 2: Table of fitted parameters of the qubits. In order to fit these parameters, we used the new model, including the kinetic inductance of the SQUID, and compared it with the values of Δ and I_p we got from the measurement.

5.3 Rabi oscillations

The frequency at which a qubit is rotating in the Bloch sphere under a resonant drive is the so called Rabi frequency Ω_R. From this frequency we can extract the length of the π and $\pi/2$ - pulses, which will be used in the next sections to analyze the relaxation and dephasing properties of the qubits. The length of the π pulse is the time it takes the to perform a half-period of the Rabi oscillations. At this time, the probability of finding the qubit is at $|e\rangle$ is $P_e = 100\%$. The $\pi/2$ pulse introduces the qubit into a coherent superposition state $(|0\rangle + |1\rangle)/\sqrt{2}$.

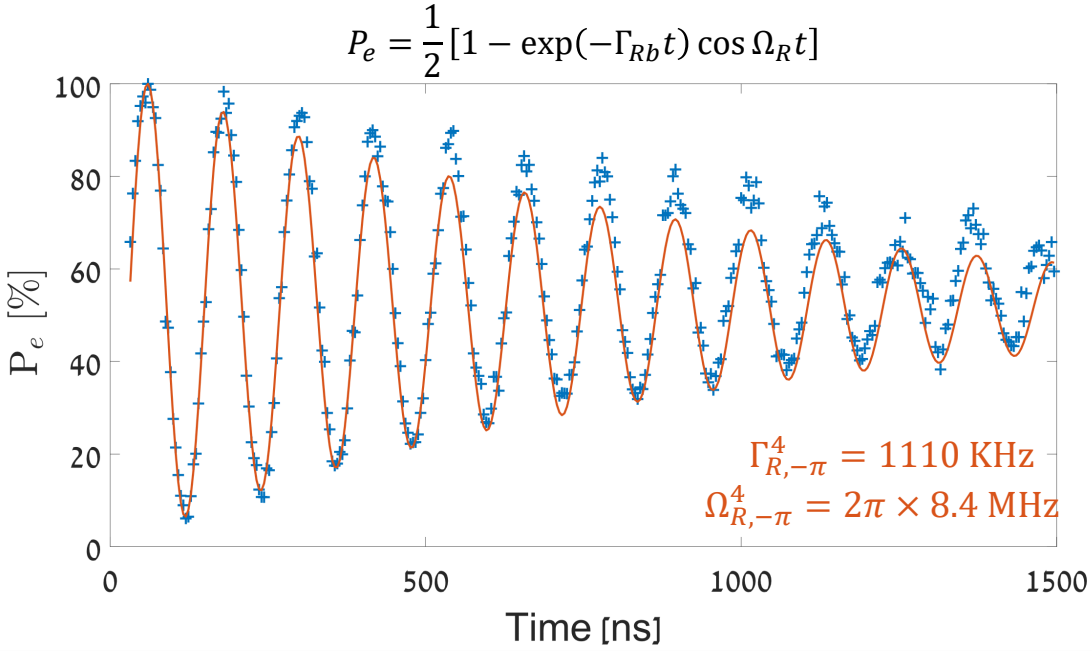

Figure 17: Rabi oscillations of qubit 4 where the blue + markers are the measurement points and the orange solid line is the fit. The probability of been in the exited state periodically oscillates between $|0\rangle$ and $|1\rangle$ at frequency $\Omega_R = 2\pi \times 8.4$MHz. For long time the qubit exponentially decays, with a typical time $\Gamma_{Rb} = 1110$KHz into a symmetric mixed state such that the probability of been in states $|0\rangle$ or $|1\rangle$ goes to 50%.

In figure 17 we present Rabi oscillations of qubit 4. The power in this experiment was set to be -83dBm and the measured Rabi frequency was $\Omega_{Rabi} = 2\pi \times 8.4$MHz. The Rabi oscillation exponentially decays due to relaxation and decoherence mechanism of the qubit.

5.4 Relaxation Rate Γ_1

The relaxation rate Γ_1 corresponds to the rate at which the qubit emits spontaneously an excitation to the environment and relaxes from the excited state $|e\rangle$ to the ground state $|g\rangle$. The probability of finding the qubit at the excited state at time t goes as [27]:

$$P_e = \exp(-\Gamma_1 t)$$

At the beginning of the experiment, the qubit was initialized at the ground state $\psi = |g\rangle$. At time $t = t_0$ a π-pulse is sent and flip the qubit to exited state $\psi = |e\rangle$. In this experiment, we change the waiting time between the π-pulse and the measurement pulse.

.

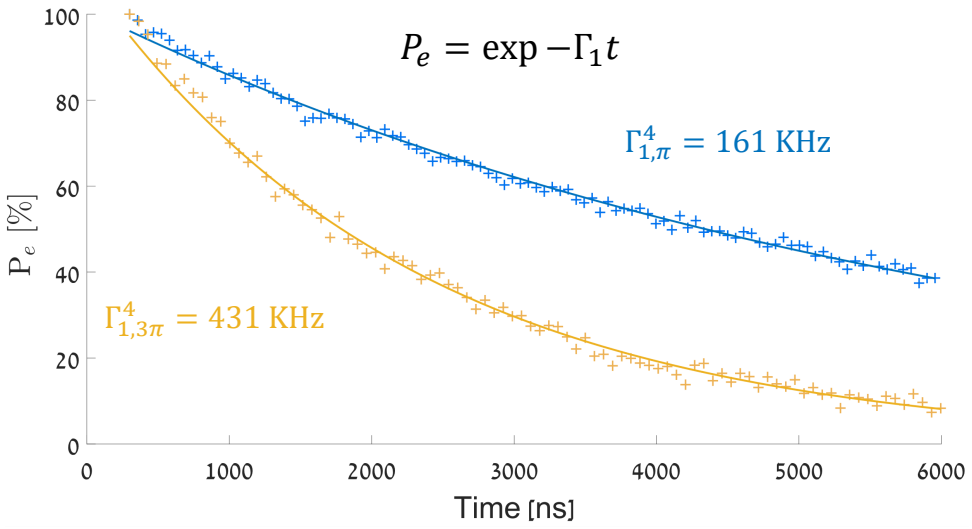

Figure 18: Relaxation experiment of qubit 4 at the optimal point $\Phi/\varphi_0 = \pi$ (blue) and $\Phi/\varphi_0 = 3\pi$ (yellow). The qubit is initialized at excited state $|e\rangle$ by a π-pulse. We present the probability of finding the qubit in the excited state at time t and fit the experimental curve to an exponential decay $P_e(t) = \exp(-\Gamma_1 t)$.

In Fig.18 we present a relaxation experiment we performed on qubit 4 at two different optimal points $\Phi/\varphi_0 = \pi$ (blue) and $\Phi/\varphi_0 = 3\pi$ (yellow). At short waiting times the probability of finding the qubit at the excited state is $P_e \sim 100\%$ for both experiments. At longer waiting time the qubit starts to relax, and the probability decreases. We see that the relaxation rate Γ_1 is much shorter at $\Phi/\varphi_0 = \pi$ than at $\Phi/\varphi_0 = 3\pi$, with fitted values of $\Gamma^4_{1,\pi} = 161$KHz and $\Gamma^4_{1,3\pi} = 431$KHz. The main reason for this is the Purcell decay as explained in Sec.1.5.

At $\Phi/\varphi_0 = \pi$ the Purcell rate $\Gamma^4_{P,\pi} = 0.84$KHz is experimentally determined by injecting the values of $\omega_{ge} = \Delta^4_\pi = 2\pi \times 4.3$GHz, $P_{in} = -83$dBm and $\Omega^2_R = 2\pi \times 8.4$MHz, obtained from the Rabi oscillations, into Eqn.26. When the qubit is at $\Phi/\varphi_0 = 3\pi$, where the parameter are $P_{in} = -115$dBm, $\Omega^2_R = 2.9$MHz, and $\omega_{ge} = \Delta^4_{3\pi} = 2\pi \times 9.35$GHz the Purcell rate become $\Gamma^4_{P,3\pi} = 325$KHz.

Magnetic flux	Qubit 1		Qubit 2		Qubit 3		Qubit 4		Qubit 5	
	Γ_1[KHz]	Γ_P[KHz]	Γ_1[KHz]	Γ_P[KHz]	Γ_1[KHz]	Γ_P[KHz]	Γ_1[KHz]	Γ_P[KHz]	Γ_1[KHz]	Γ_P[KHz]
$-\Phi_0/2$	-	-	276	32	268	32	214	0.8	313	51
$\Phi_0/2$	306	45	297	28	295	37	162	0.84	332	-
$3\Phi_0/2$	-	-	2273	33	737	623	431	325	-	-
$5\Phi_0/2$	313	211	187	43	322	85	-	-	-	-

Table 3: Γ_1 and calculated Purcell decay rate Γ_P of each measured qubit at different optimal points.

In table 3 we present the values of Γ_1 measured for each qubit as a function of the magnetic flux threading the qubit loop. The relaxation rates of qubit 2 and 3 are high, especially qubit 2. We believe that this anomaly is due to the mismatch between the frequency range of our 8-12 GHz circulator and the frequency of these qubits. An additional measurement is currently performed to assess this question.

5.5 Dephasing Rate - Γ_2

$\Gamma^\varphi_{2,R}$ - Ramsey pure dephasing rate

As mentioned earlier, the decoherence rate of a qubit Γ_2 is determined by the relaxation rate Γ_1 and the pure dephasing rate Γ^φ_2 and given by: $\Gamma_2 = \frac{\Gamma_1}{2} + \Gamma^\varphi_2$.

Therefore, we fit the probability of finding the qubit in $|g\rangle/\ |e\rangle$ state to:

$$P_{e/g} = \frac{1}{2}\left[1 \pm \cos\left(2\pi\delta_{s,q}t_r\right)\cdot \exp-\left(t\Gamma_1/2\right)\exp-\left(t\Gamma_{2,R}^{\varphi}\right)^2\right] \tag{40}$$

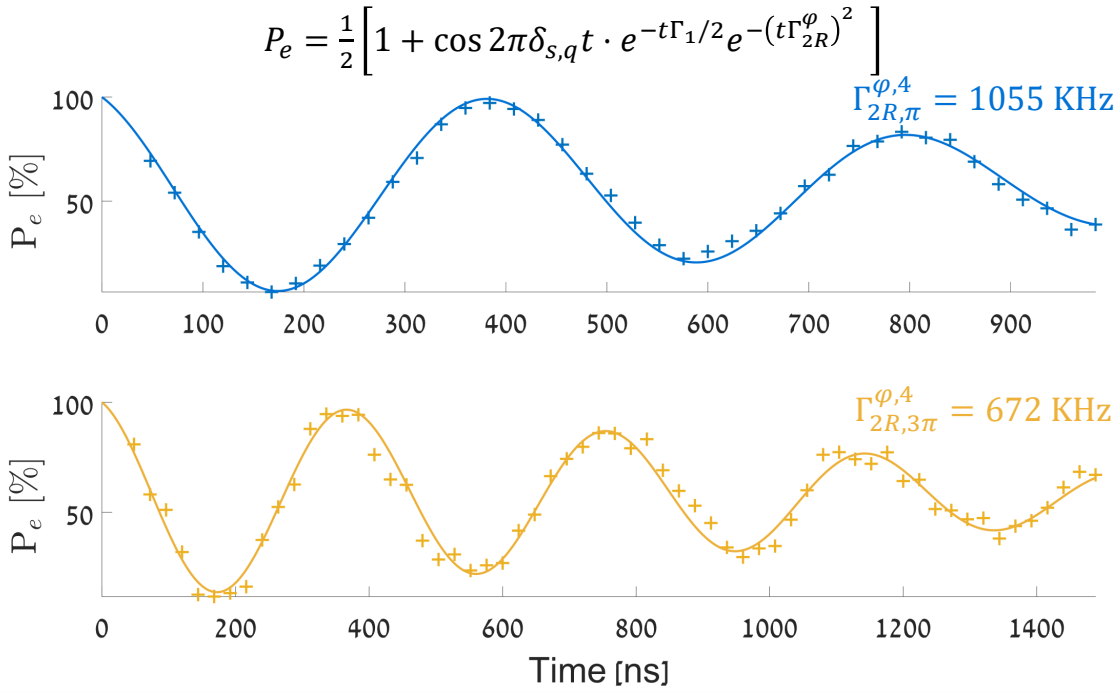

Figure 19: Ramsey experiment of qubit 4 for two optimal points $\Phi/\varphi_0 = \pi$ (top) and $\Phi/\varphi_0 = 3\pi$ (bottom) showing the probability to find the qubit at the exited state. The + signs are the measured data points and the solid line is the fit as given in Eqn.40

In Fig.19 we present the Ramsey experiment of qubit 4 at the optimal points $\Phi/\varphi_0 = \pi$ (top) and $\Phi/\varphi_0 = 3\pi$ (bottom). At $\Phi/\varphi_0 = \pi$, the pure dephasing rate ($\Gamma_{2R,\pi}^{\varphi,4} = 1055$KHz) is higher than at $\Phi/\varphi_0 = 3\pi$ ($\Gamma_{2R,3\pi}^{\varphi,4} = 672$KHz).

In the following table we present the Ramsey pure dephasing rate of each qubits for different optimal points.

$\Gamma_{2,R}^{\varphi}$[KHz]

Magnetic flux	Qubit 1	Qubit 2	Qubit 3	Qubit 4	Qubit 5
$-\Phi_0/2$	-	1025	1622	875	1194
$\Phi_0/2$	1684	-	1091	1055	1084
$3\Phi_0/2$	-	1867	868	672	-

Table 4: $\Gamma_{2,R}^{\varphi}$[KHz] of each measured qubit at different optimal points.

$\Gamma_{2,E}^{\varphi}$ - Echo pure dephasing rate

Here we follows the steps presented in Sec.1.5.

In order to take into account possible contributions of white noise and 1/f noise at first order shown in Sec.19, we fit the results by using a Voigt model:

$$P_e = \frac{1}{2}\left[1 + \exp\left(-t\Gamma_1/2\right)\exp(-\gamma t)\exp\left(-\delta^2 t^2\right)\right] \tag{41}$$

Having obtained fit parameters γ and δ, the total Echo decoherence rate Γ_{2E} corresponds to the rate at which the probability of being in state $|e\rangle$ is:

$$P_e = \frac{1}{2}\left(1 - \frac{1}{e}\right)$$

We can then extract $\Gamma^{\varphi}_{2,E}$ by simply writing $\Gamma^{\varphi}_{2,E} = \Gamma_{2E} - \Gamma_1/2$.

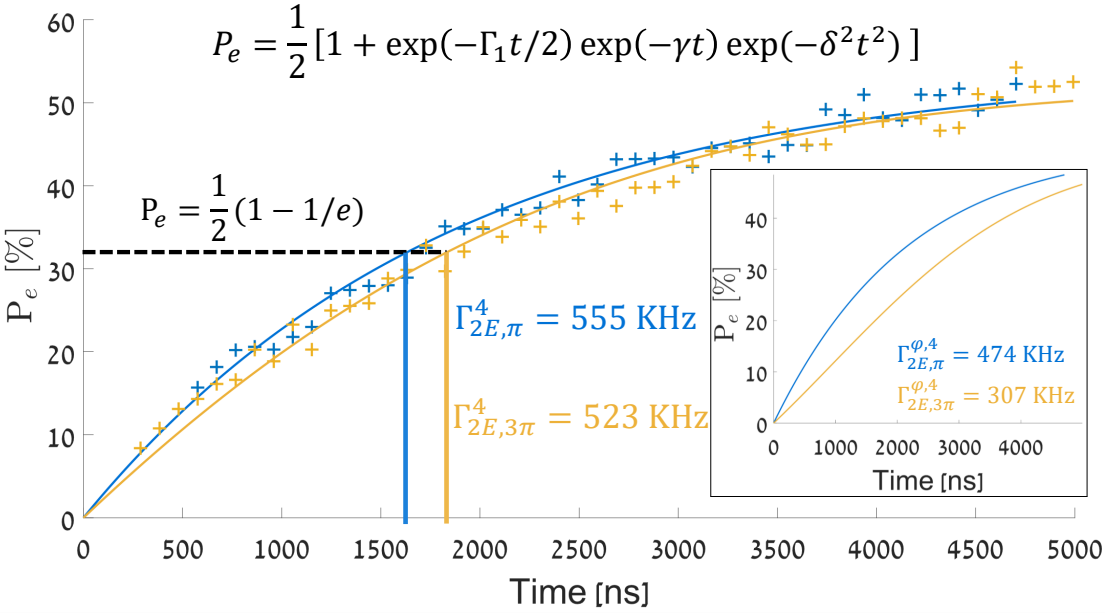

Figure 20: Echo experiment of qubit 4 at two optimal points $\Phi/\varphi_0 = \pi$ (blue) and $\Phi/\varphi_0 = 3\pi$ (yellow) showing the probability to find the qubit at the exited state as a function of time. The inset extracts the pure dephasing Γ^{φ}_2. When $\Phi/\varphi_0 = 3\pi$ the pure dephasing rate $\Gamma^{\varphi 4}_{2E,3\pi} = 307$KHz is much lower than at $\Phi/\varphi_0 = \pi$, where $\Gamma^{\varphi 4}_{2E,\pi} = 474$KHz.

In Fig.20, we present two Echo experiments performed on qubit 4 at different optimal points, namely $\Phi/\varphi_0 = \pi$ (blue) and $\Phi/\varphi_0 = 3\pi$ (yellow). The decoherence rates are almost equal, where $\Gamma^4_{2E,\pi} = 555$KHz and $\Gamma^4_{2E,3\pi} = 523$KHz. However, the pure dephasing rates change significantly with $\Gamma^{\varphi 4}_{2E,\pi} = 474$KHz vs $\Gamma^{\varphi 4}_{2E,3\pi} = 307$KHz. This behavior is due to the ratio between the SQUID and the qubit areas, as explained before.

$\Gamma^{\varphi}_{2,E}$[KHz]

Magnetic flux	Qubit 1	Qubit 2	Qubit 3	Qubit 4	Qubit 5
$-\Phi_0/2$	-	370	593	432	370
$\Phi_0/2$	384	424	408	474	493
$3\Phi_0/2$	-	1604	727	307	-

Table 5: $\Gamma^{\varphi}_{2,E}$ [KHz] of each measured qubit at different optimal points.

Table 5 presents the pure dephasing rates of the qubits at various optimal points. We see that at $\Phi/\varphi_0 = \pm\pi$, the dephasing rates are similar and much lower than the ones we got from the Ramsey sequence, ($\Gamma_{2,R}/\Gamma_{2,E} < 4.5$). Unlike in qubit 4, the dephasing rate of qubits 2 and 3 does not decrease as expected.

5.6 Flux noise amplitude

Away from the optimal point, the first order flux noise inside the qubit is the main decoherence source. Therefore, in order to evaluate the amplitude of the flux noise $\sqrt{A}$, one should fit the dephasing rate found from the echo experiment and fit them with the expression given in Eqn.29.

In Fig.21 we present $\Gamma^{\varphi}_{2,E}$ of qubit 4 as a function of ε at the vicinity of $\Phi/\varphi_0 = \pi$ and $\Phi/\varphi_0 = 3\pi$, presenting flux noise amplitude $\sqrt{A^4_{E,\pi}} = 2.76\mu\Phi_0$ and $\sqrt{A^4_{E,3\pi}} = 1.94\mu\Phi_0$, respectively.

$$\Gamma_{2,E} = \frac{2I_p}{\hbar}\sqrt{A}\sqrt{\ln 2}\,\Phi_0\varepsilon$$

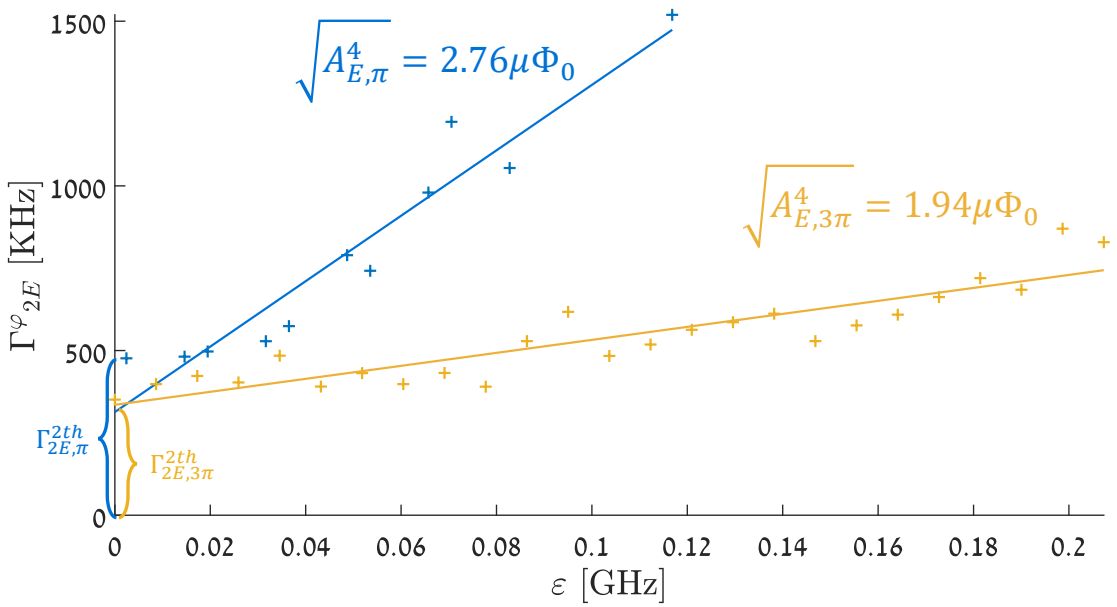

Figure 21: Decoherence rate Γ^{φ}_{2E} vs ε of qubit 4 at the optimal points $\Phi/\varphi_0 = \pi$ (blue) and $\Phi/\varphi_0 = 3\pi$ (yellow). Away from the optimal point, the dominant noise source is the first order flux noise at the qubit, consequently allowing finding the amplitude of the flux noise by using 29. When decreasing ε, the dephasing rates linearly drop to a constant higher than zero due to other decoherence mechanisms such as first-order flux noise inside the SQUID, second-order flux noise inside the qubit, photon noise, and charge noise.

Table 6 presents the flux noise amplitudes we got for each measurement.

Magnetic flux	Qubit 1	Qubit 2	Qubit 3	Qubit 4	Qubit 5
$-\Phi_0/2$	-	1.01	2.23	1.95	1.12
$\Phi_0/2$	1.94	5.15	3.27	2.76	1.92
$3\Phi_0/2$	-	-	-	1.943	-

Table 6: Flux noise amplitude: $\sqrt{A}[\mu\Phi_0]$ of each measured qubit at different optimal points.

When $\varepsilon \longrightarrow 0$, i.e., at the optimal point, the dephasing rates Γ^{φ}_2 are not going to zero, due to several mechanisms that become dominant at this point. These noise mechanisms can be divided into two categories: flux-dependents and flux-independents. The first category includes the first-order flux noise inside the SQUID and the second-order flux noise inside the qubit. The second category includes the photon noise and the charge noise, which we will not discuss.

In the following, we will evaluate the decoherence rates of qubit 4 at the optimal points due to the mechanisms mentioned above and try to determine the dominant source noise we have in our system.

1. Flux-dependent noise
   In the following we chose the amplitude of the flux noise to be $\sqrt{A} \sim 2.33\mu\Phi_0$ like we got before.

   (a) First order of flux inside the SQUID:
   By using the expression of the dephasing rate presented in Eqn.35

$$\Gamma_{2E} = 2\pi \times \delta(d) \left|\sin\frac{\Phi_S}{\varphi_0}\right| \frac{\sqrt{A\ln(2)}}{\Phi_0}$$

Qubit number	Magnetic flux	First order flux noise in SQUID [KHz]	Second order flux noise [KHz]	Photon noise [KHz]	$\Gamma^{\varphi}_{2,E}$ [KHz]
1	$\Phi_0/2$	377	49.7	5.7	384
	$3\Phi_0/2$	127	12.0	3.9	-
2	$\Phi_0/2$	373	48.5	3.2	424
	$3\Phi_0/2$	208	11.3	2.6	1604 (?)
3	$\Phi_0/2$	397	48.5	6.4	408
	$3\Phi_0/2$	46	11.6	0.9	727 (?)
4	$\Phi_0/2$	293	116.2	2.4	474
	$3\Phi_0/2$	130	22.2	50.8	307
5	$\Phi_0/2$	438	48.3	20.2	493
	$3\Phi_0/2$	102	9.8	1.6	-

Table 7: Dephasing rates due to several mechanisms while the qubit is at the optimal point.

we get that the relaxation rates of the qubit at the two optimal points shown in Fig.21 are $\Gamma^{\varphi,SQ1th}_{2E,\pi} = 293$KHz and $\Gamma^{\varphi,SQ1th}_{2E,3\pi} = 130$KHz.

(b) Second order flux noise inside the qubit:

The dephasing rate, due to this noise is given by:

$$\Gamma^{\varphi,2th}_{2E} = 451.7 \cdot 10^{-6} \cdot \frac{\left(I_P[\text{nA}]\sqrt{A}[\mu\Phi_0]\right)^2}{\Delta[\text{GHz}]}[\text{KHz}]$$

we get that $\Gamma^{\varphi,2th,4}_{2E,\pi} \sim 116$KHz and $\Gamma^{\varphi,2th,4}_{2E,3\pi} = 22$KHz.

2. Flux-independent noise

Photon noise:
The dephasing due to thermal noise in the system is given by [54]:

$$\Gamma^{photon}_{2E} = 4\left(\frac{g^2}{\Delta_R}\right)^2 \frac{Q_c}{2\omega_r}\sum_i \bar{N}_{th,i}(T_i)$$

where $\bar{N}_{th,i}(T_i)$ is the average number of photons, generated at temperature T_i having the frequency of the qubit ω_{ge}, which can be evaluated from the Bose-Einstein distribution, Eqn.39.

The dephasing of the qubit due to the thermal noise coming from all parts of our system are $\Gamma^{photon}_{2E,\pi} = 2.4$KHz and $\Gamma^{photon}_{2E,3\pi} = 51$KHz.

From table 7 we learn that while the qubit is at the optimal points $\Phi/\varphi_0 = (2n+1)\pi$ the qubit is dominated by the first order flux noise threading the SQUID's loop, as we expected it to be.

6 Discussion and Conclusion

The transmon qubits are today the most popular architecture for building superconducting quantum processors [15] [16], especially due to their long coherence times [10] and ease of use [17]. Yet, as one scales up the system, the large eigenvalue manifold of each transmon generates issues related to frequency crowding and gate fidelity. In contrast to transmons, flux qubits have intrinsically a huge anharmonicity: the higher energy levels of the system are very far from the qubit transition. Consequently, the flux qubit behaves as "true" two level systems, which limits frequency crowding issues. Moreover, they can be manipulated on a much shorter timescale and therefore could exhibit better gate fidelity. However, a good control of the

transition energy of the flux qubit is required if one wishes to build a scalable system. The aim of the thesis was to solve this issue. To date, the best published measurements of tunable flux qubits were performed by MIT in 2011 [55]. They exhibited relaxation rates and pure depahsing rates in the range of 1 MHz.

In this thesis, we design, fabricate, and measure a new design of tunable flux qubits. The tunability of the qubit is typically around $\delta \sim 5$ GHz and is obtained by replacing one of the Josephson junctions of the qubit by an asymmetric SQUID. The measured relaxation rates are $\Gamma_1 \sim 280$ KHz and the pure dephasing rates $\Gamma_{2E}^{\varphi} \sim 410$ KHz. These decoherence rates are much smaller than the state of the art [4, 55–64]. Moreover, we show that these decoherence rates are limited by first order flux noise in the SQUID loop and thus by the amplitude of the tunability $\delta(d)$.

In future experiements, we believe we can further increase the coherence properties of the qubit by reducing its tunability to the level of $\delta \sim 500$ MHz. To achieve this, we will reduce the effect of the SQUID's kinetic inductance by exchanging the positions of the big and small junctions of the SQUID. This exchange will reduce the effective area of the qubit since the current I_p is flowing mainly through the big junction of the SQUID. Moreover, we will be able to increase the effective ratio d: the small junction will be less affected than the big junction by the kinetic inductance. Direct and fast control of the qubit gap will be possible by passing a well-filtered DC line in the vicinity of the SQUID. To filter this line, we will use the homemade Eccosorb filters described in detail in Appendix 7 and a Purcell filter in order to protect the qubit from relaxation into the flux line. We believe that implementing these ideas will allow us to control the qubits gap on short time scales without affecting the flux qubit coherence properties.

7 Appendix

Fabrication and Characterization of Microwave Absorbing Low Pass Filters

In order to protect our qubits from high frequency noise, we must have a low pass filters. The I.R fillers we used in order to protect our samples inside the fridge were fabricated in this way. The second filter - eccosorb filter- will be in use when we will move foreword to next step of our experiment as described in the conclusions part.

I.R Filters:

The design of our low pass filter is based on a coax transmission line filled with an absorbing medium. In this section we will derive analytical expressions for the characteristic impedance and the power attenuation of a cylindrical coax filled with an absorbing medium as a function of frequency.

Poynting's theorem

Let's assume that we have a volume V enclosed with surface S filled with a medium characterized by its electric permittivity $\varepsilon = \varepsilon' - i\varepsilon''$ and magnetic permeability $\mu = \mu' - i\mu''$ in presence of a conduction current $\vec{J} = \sigma\vec{E}$. Using Maxwell equation, it is possible to show [65] that the divergence of the Poyting vector $P = \vec{E} \times \vec{H}^*$ is given by:

$$\nabla \cdot \left(\vec{E} \times \vec{H}^*\right) = \iota\omega \left(\varepsilon^* \left|\vec{E}\right|^2 - \mu \left|\vec{H}\right|^2\right) - \vec{E}J^*$$

By integrating this equation over the full volume V, we get:

$$\frac{1}{2}\oiint_S \vec{E} \times \vec{H}^* \cdot ds = \iota\omega \frac{1}{2}\int_V \left(\varepsilon^* \left|\vec{E}\right|^2 - \mu \left|\vec{H}\right|^2\right) dv - \frac{1}{2}\int_V \left|\vec{E}\right|^2 \cdot \sigma \, dv$$

$$\underbrace{\frac{1}{2}\oiint_S \vec{E} \times \vec{H}^* \cdot ds}_{\substack{\text{power flowing} \\ \text{through the system}}} = \iota\omega \underbrace{\frac{1}{2}\int_V \left(\varepsilon' |\vec{E}|^2 - \mu' \left|\vec{H}\right|^2\right) dv}_{\text{energy stored in the system of volume V}} \underbrace{- \omega \frac{1}{2}\int_V \left(\varepsilon'' |\vec{E}|^2 + \mu'' \left|\vec{H}\right|^2\right) dv + \frac{1}{2}\int_V \left|\vec{E}\right|^2 \cdot \sigma \, dv}_{\text{power lost by the system of volume V}} \tag{42}$$

The first term on the right hand side of the equation are the capacitance energy and the second is inductance energy of the volume:

$$W_e = \tfrac{1}{2}\mu' \textstyle\int_V \left|\vec{E}\right|^2$$

$$W_m = \tfrac{1}{2}\varepsilon' \textstyle\int_V |\vec{H}|^2$$

Assuming an homogeneous medium in the volume V, we can separate the energy loss term of previous equation into dielectric, magnetic and conductance losses as follows:

$$\boxed{P_l = P_d + P_m + P_c = \underbrace{\frac{\omega\varepsilon''}{2}\int_V |\vec{E}|^2 \, dv}_{\text{dielectric loss}} + \underbrace{\frac{\omega\mu''}{2}\int_V \left|\vec{H}\right|^2 dv}_{\text{magnetic loss}} + \underbrace{\frac{1}{2}\int_V \left|\vec{E}\right|^2 \cdot \sigma \, dv}_{\text{conductance loss}}} \tag{43}$$

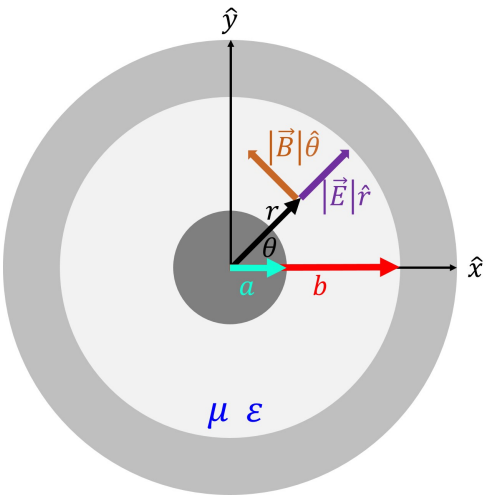

Figure 22: A 2D Illustration of the TEM mode inside a cylindrical coax filed with magnetic/dielectric medium.

Characteristic impedance:

The characteristic impedance of a coax is determined by the geometry of the coax, the electric permittivity ε and the magnetic permeability μ of its filling medium. It is defined as $Z_0 = \sqrt{\mathcal{L}/\mathcal{C}}$, the ratio between the inductance and the capacitance per unit length of the coax. For low loss medium the value of the characteristic impedance should be matched as much as possible to 50Ω if one wishes to avoid reflections of the filter back to the transmission line. In the following, we

will evaluate the characteristic impedance of an infinite cylindrical coax filled with an homogeneous medium as represented in Fig.22.

As shown In Fig.22, the TEM mode of a cylindrical coax is such that the electric field is radial while the magnetic field is azymutal [65]. Inside the medium, the charge density is zero, therefore by writing Gauss law with cylindrical coordinates we get:

$$\frac{1}{r}\frac{\partial}{\partial r}\left(r\vec{E}\right) = 0 \Longrightarrow E_0 = A/r$$

which implies that

$$V = \int_a^b \vec{E}\cdot dl \Longrightarrow A = V_0/\ln(b/a)$$

The magnetic field can be found by using Ampere's law $\int \vec{H}\cdot dl = I$:

$$\vec{H} = \frac{I_0}{2\pi r}\hat{\theta}$$

In order to express the inductance and the capacitance of the coax, we shall remember that the energy stored due to inductance and capacitance is:

$$W_m \equiv \tfrac{1}{2}L\left|I_0\right|^2$$

$$W_e \equiv \tfrac{1}{2}C\left|V_0\right|^2$$

Therefore, we get that the inductance and the capacitance per unit length of the coax are:

$$\mathcal{L} = L/z = \tfrac{\mu'}{|I_0|^2}\int_S \left|\vec{H}\right|^2$$

$$\mathcal{C} = C/z = \tfrac{\varepsilon'}{|V_0|^2}\int_S \left|\vec{E}\right|^2$$

The characteristic impedance is given by[5]:

$$\boxed{Z_0 = \sqrt{\mathcal{L}/\mathcal{C}} = \frac{1}{2\pi}\sqrt{\frac{\mu'}{\varepsilon'}}\ln\left(\frac{b}{a}\right)} \tag{44}$$

Absorption of a coax cable

Due to the loss mechanisms mentioned herein above, the power of an incoming electromagnetic wave will decrease exponentially as the wave progresses in the medium:

$$P(z) = P_0 e^{-2\alpha z}$$

where P_0 is the power of the incoming electromagnetic wave at $z = 0$ and α is the attenuation constant. The incoming power P_0 corresponds to the flux of the Poynting vector at $z = 0$.

$$P_0 = \frac{1}{2}\mathrm{Re}\left[\int E\hat{r} \times H\hat{\theta}\right] = \frac{1}{2}\mathrm{Re}\left[\int_a^b \int_0^\pi \frac{V_0}{r\ln(\frac{b}{a})}\frac{I_0\mu}{2\pi r} r dr d\theta\right] = V_0 I_0 = \frac{1}{2}\frac{V_0^2}{Z_0}$$

Now, we will find an expression of the attenuation constant α. The power loss per length unit $P_l(z)$ is given by:

$$P_l(z) = -\frac{dP}{dz} = 2\alpha P_0 e^{-2\alpha z} = 2\alpha P(z)$$

therefore we can write:

$$\alpha = \frac{P_l(z)}{2P(z)} = \frac{P_l(z=0)}{2P(z=0)} = \frac{P_l(z=0)}{2P_0} \tag{45}$$

In the following we will evaluate the contribution of the different loss mechanisms mentioned in Sec.1.2 for the case a cylindrical coax.

The conductance loss of the filter are due to the current flowing at the surface of the metal surrounding the coax. The metal used to fabricate the filters is copper and can be safely considered as a **good conductor.** The skin depth given in table 8 corresponds to the region where the electromagnetic field can penetrate in the metal. For copper at 10 GHz, $\delta_s \sim 6.6 \cdot 10^{-7}$m which is very small compared to the wavelength we consider. Therefore, at high frequencies, one can consider that the current density $\vec{J}$ is uniform in the segment $0 < r < \delta_s$ and zero outside.

$$\vec{J} = \begin{cases} \frac{J_s}{\delta_s}\hat{r} & 0 < r < \delta_s \\ 0 & r > \delta_s \end{cases}$$

Therefore, we get

$$P_c = \frac{\sigma}{2}\int_S \int_{z=0}^{\delta_s} |E|^2 \, dr\, ds = \frac{1}{2\sigma}\int_S \int_{r=0}^{\delta_s} \left|\frac{\vec{J}_s}{\delta_s}\right|^2 dr\, ds = \frac{1}{2\sigma\delta_s}\int_S \left|\vec{J}_s\right|^2 ds = \frac{R_s}{2}\int_S \left|\vec{J}_s\right|^2 ds = \frac{R_s}{2}\int_S \left|\vec{H}\right|^2 ds$$

where $R_s = \sqrt{\frac{\omega\mu}{2\sigma}}$ is the surface resistance of the metal. At 10 GHz, this resistance is $R_s = 0.026\,\Omega$. For a cylindrical coax, we get

$$P_{lc} = \frac{R_s}{2}\int_S \left|\vec{H}\right|^2 = \frac{R_s}{2}\int_0^1 \int_0^{2\pi} \left(\frac{V_0}{2\pi Z_0 a}\right)^2 a d\theta dz + \frac{R_s}{2}\int_0^1 \int_0^{2\pi} \left(\frac{V_0}{2\pi Z_0 b}\right)^2 b d\theta dz = \frac{R_S\left|V_0^2\right|}{4\pi Z_0^2}\left(\frac{1}{a} + \frac{1}{b}\right)$$

[5] In high losses coax the characteristic impedance is complex $Z_0 = \frac{1}{2\pi}\sqrt{\frac{\mu' + \iota\mu''}{\varepsilon' + \iota\varepsilon''}}\ln\left(\frac{b}{a}\right)$.

Quantity	General lossy medium	Good conductor ($\sigma \gg \omega\varepsilon'$)
Complex propagation constant	$\iota\omega\sqrt{\mu\varepsilon}$	$(1+\iota)\sqrt{\omega\mu\sigma/2}$
skin depth	$1/\mathrm{Re}[\iota\omega\sqrt{\mu\varepsilon}]$	$\sqrt{2/\omega\mu\sigma}$
Relative dielectric permittivity	$(\varepsilon' - i\varepsilon'')/\varepsilon_0$	$\frac{i\sigma}{\omega\varepsilon_0}$
Relative magnetic permeability	$(\mu' + \mu'')/\mu_0$	1

Table 8

For a cylindrical coax, the dielectric losses per unit length can be calculated straightforwardly :

$$P_d = \frac{\omega\varepsilon''}{2}\int_V \left|\vec{E}\right|^2 dv = \frac{\omega\varepsilon''}{2}\int_0^1\int_a^b\int_0^{2\pi}\left(\frac{V_0}{r\ln\frac{b}{a}}\right)^2 rd\theta dr dz = \frac{\omega\varepsilon''}{\ln\frac{b}{a}}V_0^2$$

The same can be done for magnetic losses per unit length and we get:

$$P_m = \frac{\omega\mu''}{2}\int_V \left|\vec{H}\right|^2 dv = \frac{\omega\mu''}{2}\int_0^1\int_a^b\int_0^{2\pi}\left(\frac{V_0}{2\pi Z_0 r}\right)^2 rd\theta dr = \frac{\omega\mu''}{4\pi Z_0^2}\ln\frac{b}{a}V_0^2$$

And therefore we get the following loss rates[6]:

$$\alpha_d = \frac{P_d}{2P_0} = \sqrt{\frac{\mu'}{\varepsilon'}}\frac{\omega\varepsilon''}{2}$$

$$\alpha_m = \frac{P_m}{2P_0} = \sqrt{\frac{\varepsilon'}{\mu'}}\frac{\omega\mu''}{2}$$

$$\alpha_c = \frac{P_c}{2P_0} = \sqrt{\frac{\varepsilon'}{\mu'}}\frac{R_s}{2\ln(b/a)}\left(\frac{1}{a}+\frac{1}{b}\right)$$

Eccosorb filters

The Eccosorb filters have widely used on the field of superconducting qubits [66–69]. In our system, their goal is to eliminate any high frequency noise coming from the environment to the flux line. We control the flux qubit using a DC current flowing inside the flux line, therefore, a low pass filter is needed.

In the previous section we derived analytical expressions for a cylindrical coax. In the following we will use these expressions in order to estimate the expected attenuation values and compare them to the experiment.

We use is "*Eccosorb - CRS117*" by *LAIRD R&F products INC*. It is a dark-gray epoxy, magnetically loaded, with high loss at the high microwave frequencies range. It has high flexibility properties due to RTV silicone rubber materials floating inside the mixture.

The electric properties of Eccosorb-CRS117 are given in table 9 and in Fig 23a (23b) .

[6] In high losses α_d, α_m, $\alpha_c$are taken to be the of real prat of complex expressions. This complex term is a direct result of using the complex characteristic impedance

parameter\GHz	10^{-7}	10^{-6}	10^{-5}	10^{-4}	10^{-3}	10^{-2}	10^{-1}	1	3	8.6	10	18.0
$\varepsilon'/\varepsilon_0$	195	158	120	58	62	48	38	28	22.9	21.4	21	20.6
$\varepsilon''/\varepsilon_0$	35	33	28	20	14	8.6	4.6	2.5	1.4	0.42	0.42	0.41
μ'/μ_0	5	5	5	5	5	5	4.8	4.1	3.4	1.2	1.1	1.0
μ''/μ_0	0	0	0	0	0	0	0.48	0.82	1.33	13	1.38	2
S_{21}[db/cm]	0	0	0	0	0	0.03	0.27	2.8	11.0	46	56	119

Table 9: The Electric and magnetic properties of the Eccosorb CRS117 as given in [70]. The real and the imaginary parts of permittivity ε are given by ε' and ε''. The real and the imaginary parts of permeability μ are given by μ' and μ''.

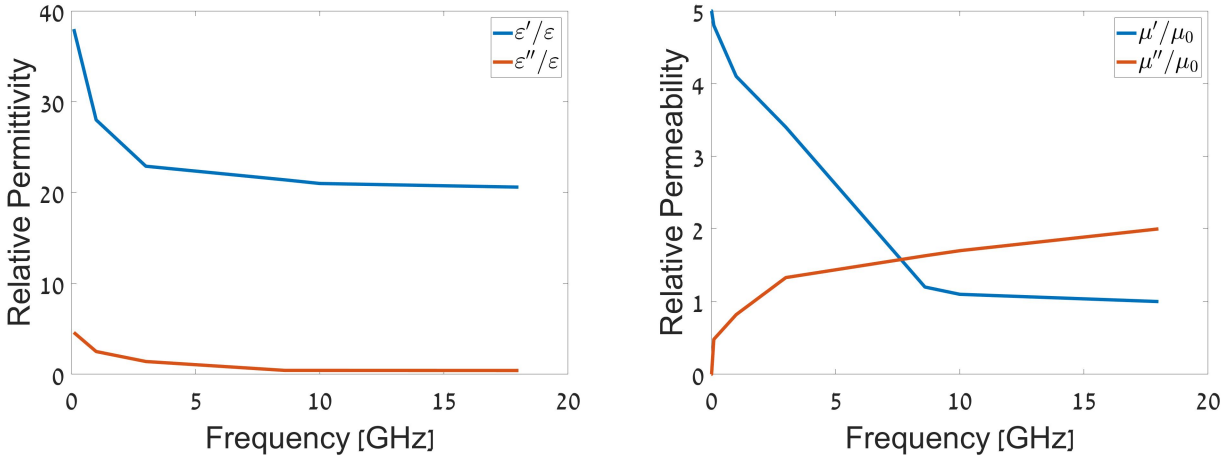

(a) (b)

Figure 23: (a) The values of the relative permittivity of Eccosorb CRS117 as a function of frequency. The blue represents the real part (ε') and the orange represents the imaginary part (ε''). (b) The values of the relative permeability of the Eccosorb as a function of frequency. The blue represents the real part (μ') and the orange represents the imaginary part (μ'').

Eccosorb filter fabrication recipe

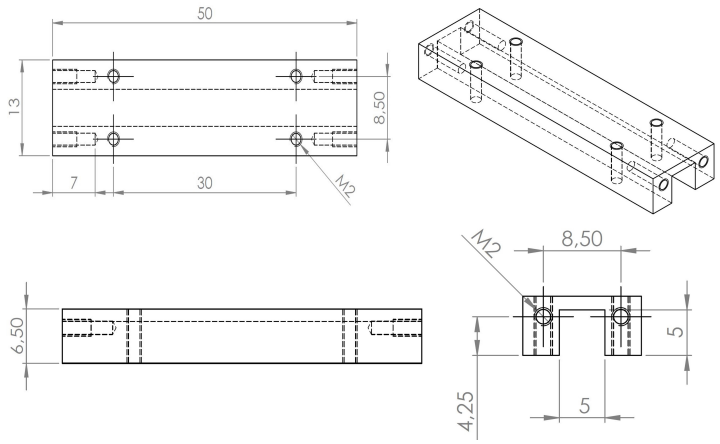

Figure 24: Cross sectional view of the Eccosorb filter.

Our filters consists of a 50 mm-long box made out of oxygen free (OHFC) copper coated with gold (3 microns copper + 0.7 microns gold). The height of the box is 10mmand its width is 5mm as shown in the figure below. The internal conductor of the coax is made out of a copper wire of 0.4 mm diameter.

Fabrication recipe:

Step #	Process name	About the process	Additional figure
1	Filter preparation	Close the edges and shut the holes with duct tape to prevent the Eccosorb from escaping.	
2	Prepare the connectors	Remove the cover from the copper wire.	
		Solder the copper wire to the SMA connector.	
3	Mixture preparation	Pour 20g per filter of resin (Part A) on a plate.	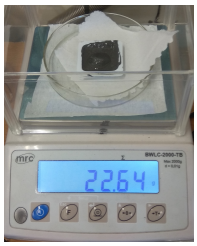
		Add the catalyst (Part B) using a syringe to a plate, such that the weight ratio between them is $W_A : W_B = 1 : 118$. The total weight of the mixture after you will add part B is $W_{tot} = W_A \left(1 + \frac{1.18}{100}\right)$	
		Blend until the mixture has a uniform texture.	
		Insert the plate into a vacuum chamber for ~10 minutes at $10^{-3} mbar$.	
4	Filling the Filters	Fill the filters with the Eccosorb mixture, until it covers about 2mm above the metal surface.	
5	Air removal	Insert into a vacuum chamber for 30-45 minutes.	
		Take out the filters and tap them on a flat surface. It helps to increase the density of the Eccosorb.	
6	Mixture drying	Leave the filter on shivering plate over a night. It releasing the bubbles that are still stuck inside the Eccosorb mixture.	
7	Cleaning	Remove the leftovers from the filter. But keep the middle strip $100\mu m$ higher than the metal surface.	
8	Close the filter	Add the SMA connectors one on each side.	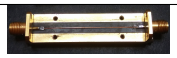
		Close the box with its complementary half. It is recommended to use clamps in order to achieve a good closing.	

Characteristic impedance

In the following we compare the characteristic impedance of the Eccosorb filters with what is expected from the electromagnetical properties provided by *LAIRD* company.

Since our filter has a rectangular shall shape, there is no analytical expression for the magnetic field inside it. Therefore, in order to detemine the parametres of the coax, hight, width, and internal core we use *HSFF* ($3D$ numerical microwave simulator).

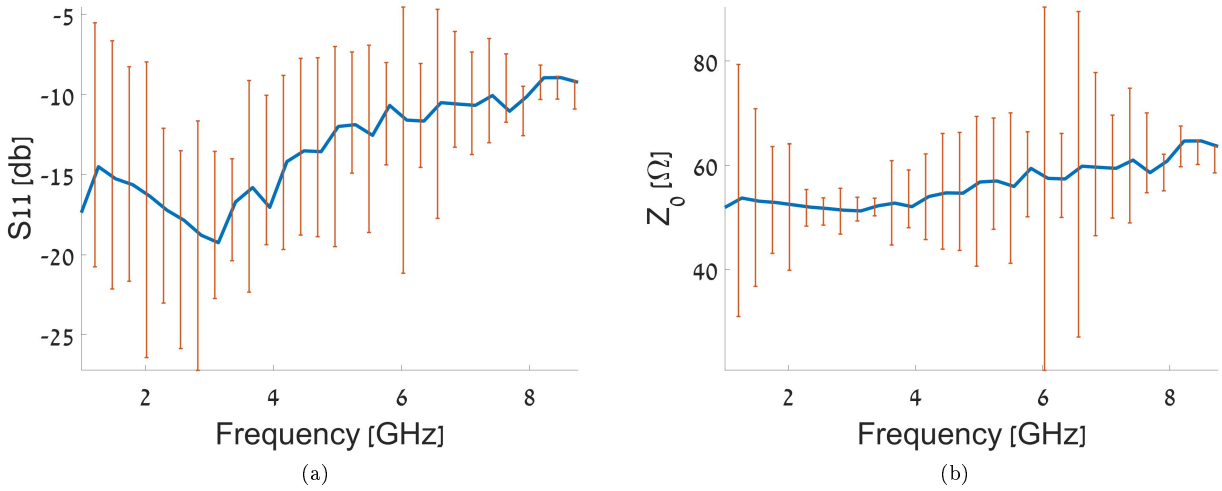

(a) (b)

Figure 25: (a) S_{11}as a function of the frequency of the incident wave. (b) The characteristic impedance Z_0 of the coax as a function of the frequency.

In Fig 25 we show the reflection coefficient and the characteristic impedance of the Eccosorb filters versus frequency.

Power attenuation

In Fig.26a we show the attenuation coefficient determined Eq. 43 and using the parameters of Eccosorb given in table 8. We see that the magnetic losses are the major source of loss.

In Fig.26b, we show the data summarizing the attenuation of 11 filters measured at room temperature and compare with its theoretical estimation. Although the attenuation is very strong, at high frequencies, its much smaller than the expected attenuation presented in the datasheet 9.

After measuring and estimate the filling fraction of the air inside the mixture (about 2%) and running a numerical simulation of our square coax using *HSFF*, which perfectly matched the expected attenuation. We suggest that, the inconsistent is a result of some curvature in the inner core of the coax. As a result, the propagating waves are no no longer TEM waves.

Copper Powder filters

Copper powder filers are commonly used on the $CQED$ filed and especially on the field of superconducting qubits readout [71–73]. These filters are usually connected to the input and output ports of the resonator and are used in order to attenuate very high frequencies, correspond to higher mods of the resonator. Therefore, in our situation, we should design a filter that have small attenuation up to 10GHz frequencies and strong absorbance on the

The copper powder filter's internal medium consists of (epoxy) mixture of black stycast (Henkel) and copper powder. The stycast is non magnetic substance $\mu'_h/\mu_0 = 1$, and having an almost constant permittivity $\varepsilon'_h/\varepsilon_0 \sim 6$ for frequencies < 25GHz [74, 75]. The copper, however, is a good conductor, therefore, its permittivity is purely imaginary ($\varepsilon''_i = \frac{i\sigma}{\omega}$). As a result, a penetrating electromagnetic field, into the copper, is quickly absorbed after a typical distance called the *skin dept* δ_S (See table 8). Therefore, copper grains with an average diameter $d > \delta_S$ will fully absorb any incoming electromagnetic flied. Accordingly, there is a linear relation between the absorption capability and the filling fraction of the copper grains in the volume. In our case, we want to absorb high frequencies > 10GHz, so the maximal skin depth is $\delta_s = \sqrt{2/\omega\mu\sigma} \approx 0.6\mu$m. Thus, we are working with copper grains with average diameter of few microns $< 45\mu$m.

In order to estimate the effective permittivity of the stycast-copper powder mixture, we used *Maxwell-Garnet's effective medium theory* [76] [77]:

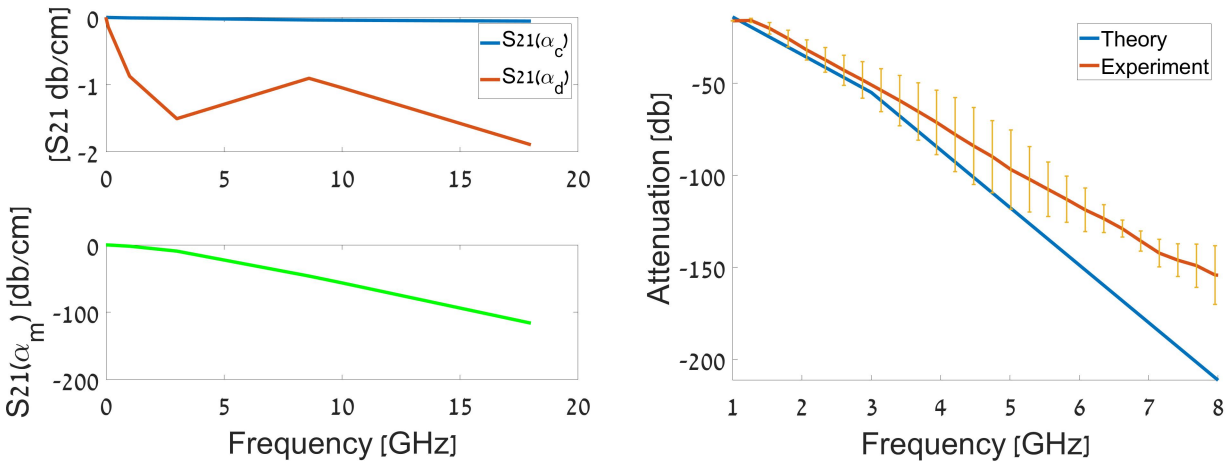

(a) (b)

Figure 26: (a) Attenuation of an Eccosorb filter due to conductance loss (blue), dielectric loss (brown), and magnetic loss (green). (b) Average attenuation of the 11 filters fabricated in the lab and the theoretical curve expected from the datasheet of *LAIRD*.

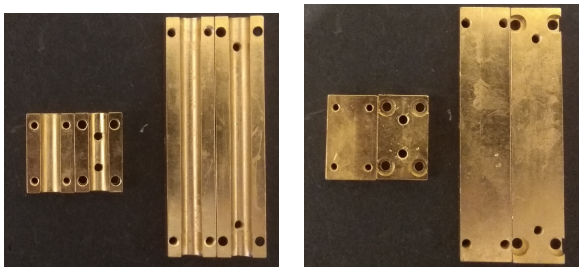

(a) (b)

Figure 27: In the figures we can see the shells of the short (left) and the long (right) filters. In (a) the outer shell of the filters shaped as a box. And in (b) the internal shell of the filters shaped as a cylinder.

$$\frac{\varepsilon_{eff} - \varepsilon_h}{\varepsilon_{eff} + 2\varepsilon_h} = f \frac{\varepsilon_i - \varepsilon_h}{\varepsilon_i + 2\varepsilon_h} \tag{46}$$

where f is the filling fraction of the inclusion medium (copper powder) , ε_i is the permittivity of the copper powder, ε_h is the permittivity of the stycast and ε_{eff} is the effective permittivity of the mixture. In this section, we will use the analytical expressions for a cylindrical coax derived in Sec.7 and the calculated effective permittivity of the mixture in order to determine the expected attenuation values and compare them to the experiment.

Copper Powder filter fabrication recipe

Our long (short) filters consists of a 60 mm-long (20mm-long) cylinder made out of oxygen free (OHFC) copper coated with gold (3 microns copper + 0.7 microns gold). The its diameter is 5mm and its internal conductor of the coax is made out of a copper wire of 0.4 mm diameter. It has two different connectors for the input and the output signals: SMA male-male and SMA male-female connectors.

In the following we will describe our recipe in order to get a filter with characteristic impedance of 50Ω.

Technical details:

Object name	Company	Mass density [g/cm^3]	Additional information
stycast 2850 FT	Henkel	2.4	The mass mixing ratio is 100:8 [74]
catalyst 24LV	Henkel	1	
Ecka kupfer AK	ECKA Granules Germany GmbH	8.96	Grain size $< 45\mu$m
In order to get 50Ω filter, the filing fraction (in volume) of the copper powder inside the media is need to be 15%.			

Fabrication recipe:

Step #	Process name	About the process	Additional figure
1	Check	Make sure that the diameter of connectors is perfectly fits to the one of the shell of the filter. If not, carve the shell to the right diameter.	
2	Connectors preparation	Remove the cover from the copper wire.	
		Solder the copper wire to the male-male connector.	
		Solder the second edge of the copper wire to the male-female connector.	
		Place the connectors inside the shell without the holes. Make sure that everything is clean.	
3	Mixture preparation	First determine the minimal total volume of the filters you make: $V_{min} = n(0.25)^2\pi * 6$. where n in the number of filters you make.	
		Pull some stycast into a plastic cup and measure its weight: The volume is calculated as: $V = 108\frac{M_{sty-A}}{100 \cdot 0.85 \cdot 2.4}$	
		Add catalyst 24LV to the cup such that the total mass will be: $M_{sty+cat} = M_{sty-A} + \frac{8}{108} \cdot 0.85 \cdot 1 \cdot V$	
		Add the copper powder such that the total mass will be: $M_{tot} = M_{sty+cat} + 0.15 \cdot 8.96 \cdot V$	
		Mix it well, until you get uniform texture	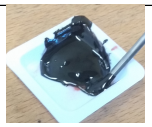
		Enter the mixture into a vacuum chamber (10^{-3}mbar) for about 10 minutes	
		Put the mixture into a syringe.	
4	Filter filling	Fill the half having the connectors with the mixture.	
		Close the filter, carefully add the second half of filters and thigh with screws.	
		Fill the filter, from one of the centered holes, using the syringe.	
		shut the holes with screws.	
5	Impedance Check	Check that you get characteristic impedance around $40\Omega - 50\Omega$. If not, clean everything and redo all over again.	
6	Mixture drying	Let it dry over night.	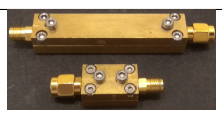

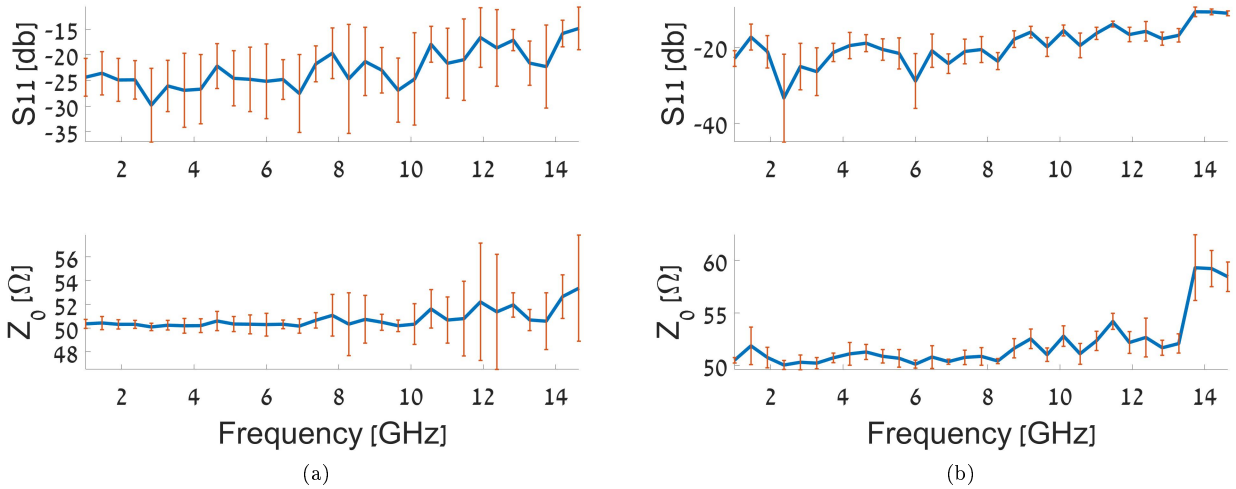

Figure 28: (a) Reflection and characteristic impedance of the long copper powder filter.(b) Reflection and characteristic impedance of the short copper powder filter.

Characteristic impedance

In the following we will discus on our experimental results for the two kinds of copper powder filters, short (20mm) and long (60mm). Using Eq. 46 we founded that a filling fraction of 15% should give us an impedance close to 50Ω with the geometry described herein above.

In Fig.28 are given the typical reflection and the characteristic impedance of our long and the short filters. We see that the characteristic impedance is close to 50Ω as desired, especially at the frequencies below 10GHz.

Power attenuation

In the following we present our experimental results for the power attenuation of the two kinds of copper powder filters, short and long. In Fig 29 we present both theoretical attenuation and experimental results. We see that there is a roughly 1db deference between the theory and the experimental results. It can be explained by some milligrams deviation of the mass ratios of the the copper and the stycast.

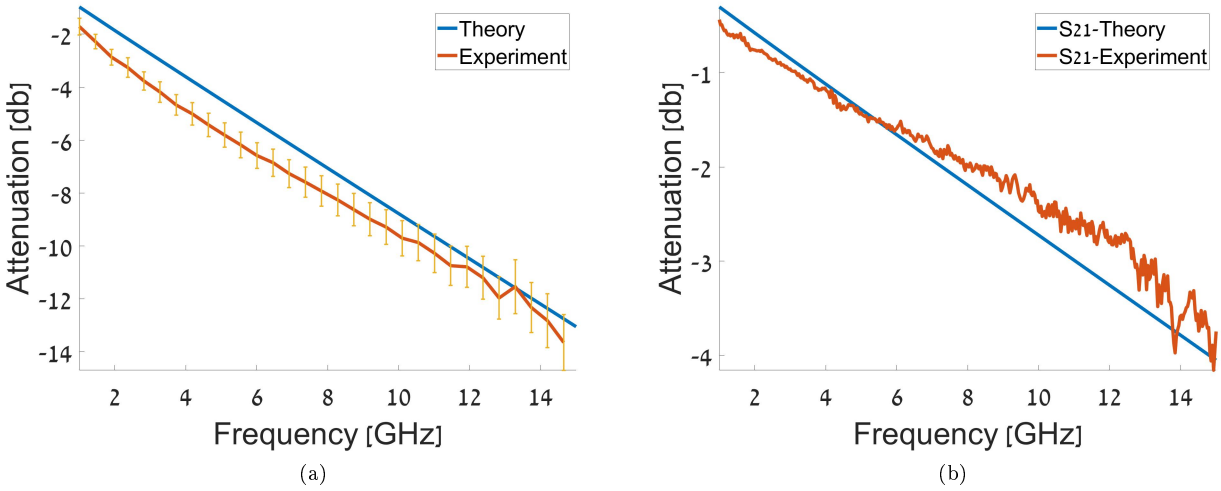

(a) (b)

Figure 29: (a) S_{21} of the long copper powder filters. (b) S_{21} of the short copper powder filters.

References

[1] Michael Stern, Gianluigi Catelani, Yuimaru Kubo, Cecile Grezes, Audrey Bienfait, Denis Vion, Daniel Esteve, and Patrice Bertet. Flux qubits with long coherence times for hybrid quantum circuits. *Physical review letters*, 113(12):123601, 2014. i, 1, 6, 7, 8, 12

[2] Jonas Bylander, Simon Gustavsson, Fei Yan, Fumiki Yoshihara, Khalil Harrabi, George Fitch, David G Cory, Yasunobu Nakamura, Jaw-Shen Tsai, and William D Oliver. Noise spectroscopy through dynamical decoupling with a superconducting flux qubit. *Nature Physics*, 7(7):565, 2011. i, 8

[3] Michael Stern. Tunable flux qubits for scalable quantum processors. i

[4] FG Paauw, A Fedorov, CJP M Harmans, and JE Mooij. Tuning the gap of a superconducting flux qubit. *Physical review letters*, 102(9):090501, 2009. i, 10, 34

[5] Peter W. Shor. Polynomial-time algorithms for prime factorization and discrete logarithms on a quantum computer. *SIAM Journal on Computing*, 26(5):1484–1509, Oct 1997. 1

[6] Lov K. Grover. A fast quantum mechanical algorithm for database search, 1996. 1

[7] Michael A Nielsen and Isaac Chuang. Quantum computation and quantum information, 2002. 1

[8] Yu Nakamura, Yu A Pashkin, and Jaw Shen Tsai. Coherent control of macroscopic quantum states in a single-cooper-pair box. *nature*, 398(6730):786–788, 1999. 1

[9] Denis Vion, A Aassime, Audrey Cottet, Pl Joyez, H Pothier, C Urbina, Daniel Esteve, and Michel H Devoret. Manipulating the quantum state of an electrical circuit. *Science*, 296(5569):886–889, 2002. 1

[10] Hanhee Paik, DI Schuster, Lev S Bishop, G Kirchmair, G Catelani, AP Sears, BR Johnson, MJ Reagor, L Frunzio, LI Glazman, et al. Observation of high coherence in josephson junction qubits measured in a three-dimensional circuit qed architecture. *Physical Review Letters*, 107(24):240501, 2011. 1, 33

[11] Yu Chen, C Neill, P Roushan, N Leung, M Fang, R Barends, J Kelly, B Campbell, Z Chen, B Chiaro, et al. Qubit architecture with high coherence and fast tunable coupling. *Physical review letters*, 113(22):220502, 2014. 1

[12] JE Mooij, TP Orlando, L Levitov, Lin Tian, Caspar H Van der Wal, and Seth Lloyd. Josephson persistent-current qubit. *Science*, 285(5430):1036–1039, 1999. 1

[13] I Chiorescu, P Bertet, K Semba, Y Nakamura, CJPM Harmans, and JE Mooij. Coherent dynamics of a flux qubit coupled to a harmonic oscillator. *Nature*, 431(7005):159, 2004. 1

[14] Vladimir E Manucharyan, Jens Koch, Leonid I Glazman, and Michel H Devoret. Fluxonium: Single cooper-pair circuit free of charge offsets. *Science*, 326(5949):113–116, 2009. 1

[15] Frank Arute, Kunal Arya, Ryan Babbush, Dave Bacon, Joseph C Bardin, Rami Barends, Rupak Biswas, Sergio Boixo, Fernando GSL Brandao, David A Buell, et al. Quantum supremacy using a programmable superconducting processor. *Nature*, 574(7779):505–510, 2019. 1, 33

[16] Petar Jurcevic, Ali Javadi-Abhari, Lev S Bishop, Isaac Lauer, Daniela F Bogorin, Markus Brink, Lauren Capelluto, Oktay Günlük, Toshinari Itoko, Naoki Kanazawa, et al. Demonstration of quantum volume 64 on a superconducting quantum computing system. *Quantum Science and Technology*, 6(2):025020, 2021. 1, 33

[17] Rami Barends, Julian Kelly, Anthony Megrant, Daniel Sank, Evan Jeffrey, Yu Chen, Yi Yin, Ben Chiaro, Josh Mutus, Charles Neill, et al. Coherent josephson qubit suitable for scalable quantum integrated circuits. *Physical review letters*, 111(8):080502, 2013. 1, 33

[18] TA Fulton and LN Dunkleberger. Lifetime of the zero-voltage state in josephson tunnel junctions. *Physical Review B*, 9(11):4760, 1974. 4

[19] Michael Tinkham. *Introduction to superconductivity*. Courier Corporation, 2004. 4, 10

[20] Floortje Geertruida Paauw. *Superconducting flux qubits: Quantum chains and tunable qubits*. PhD thesis, 2009. 4

[21] H Tanaka, Y Sekine, S Saito, and H Takayanagi. Dc-squid readout for qubit. *Physica C: Superconductivity*, 368(1-4):300–304, 2002. 5

[22] Hideaki Takayanagi, Hirotaka Tanaka, Shiro Saito, and Hayato Nakano. Readout of the qubit state with a dc-squid. *Superlattices and microstructures*, 32(4-6):221–229, 2002. 5

[23] Pieter Cristiaan De Groot. *Coupled flux qubits and double bifurcation readout*. PhD thesis, 2010. 5

[24] Edwin T Jaynes and Frederick W Cummings. Comparison of quantum and semiclassical radiation theories with application to the beam maser. *Proceedings of the IEEE*, 51(1):89–109, 1963. 5

[25] Agustin Palacios-Laloy. *Superconducting qubit in a resonator: test of the Legget-Garg inequality and single-shot readout*. PhD thesis, 2010. 6, 24

[26] Alexandre Blais, Ren-Shou Huang, Andreas Wallraff, Steven M Girvin, and R Jun Schoelkopf. Cavity quantum electrodynamics for superconducting electrical circuits: An architecture for quantum computation. *Physical Review A*, 69(6):062320, 2004. 6

[27] Serge Haroche and J-M Raimond. *Exploring the quantum: atoms, cavities, and photons*. Oxford university press, 2006. 6, 28

[28] Ioan M Pop, Kurtis Geerlings, Gianluigi Catelani, Robert J Schoelkopf, Leonid I Glazman, and Michel H Devoret. Coherent suppression of electromagnetic dissipation due to superconducting quasiparticles. *Nature*, 508(7496):369, 2014. 7

[29] Juha Leppäkangas and Michael Marthaler. Fragility of flux qubits against quasiparticle tunneling. *Physical Review B*, 85(14):144503, 2012. 7

[30] Simon Gustavsson, Fei Yan, Gianluigi Catelani, Jonas Bylander, Archana Kamal, Jeffrey Birenbaum, David Hover, Danna Rosenberg, Gabriel Samach, Adam P Sears, et al. Suppressing relaxation in superconducting qubits by quasiparticle pumping. *Science*, 354(6319):1573–1577, 2016. 7

[31] Fei Yan, Simon Gustavsson, Archana Kamal, Jeffrey Birenbaum, Adam P Sears, David Hover, Ted J Gudmundsen, Danna Rosenberg, Gabriel Samach, Steven Weber, et al. The flux qubit revisited to enhance coherence and reproducibility. *Nature communications*, 7(1):1–9, 2016. 7

[32] G. Catelani, R. J. Schoelkopf, M. H. Devoret, and L. I. Glazman. Relaxation and frequency shifts induced by quasiparticles in superconducting qubits. *Phys. Rev. B*, 84:064517, Aug 2011. 7

[33] Chunqing Deng, Martin Otto, and Adrian Lupascu. An analysis method for transmission measurements of superconducting resonators with applications to quantum-regime dielectric-loss measurements. *Journal of Applied Physics*, 114(5):054504, 2013. 7

[34] Aaron D OâConnell, M Ansmann, Radoslaw C Bialczak, Max Hofheinz, Nadav Katz, Erik Lucero, C McKenney, Matthew Neeley, Haohua Wang, Eva M Weig, et al. Microwave dielectric loss at single photon energies and millikelvin temperatures. *Applied Physics Letters*, 92(11):112903, 2008. 7

[35] Tikai Chang. Coupling single spins to ux qubits, 2017. 7

[36] Crispin W Gardiner and Matthew J Collett. Input and output in damped quantum systems: Quantum stochastic differential equations and the master equation. *Physical Review A*, 31(6):3761, 1985. 7

[37] CW Gardiner and P Zoller. Quantum noise, springer-verlag, berlin (2000. 2004. 7

[38] Daniel F Walls and Gerard J Milburn. *Quantum optics*. Springer Science & Business Media, 2007. 7

[39] Howard M Wiseman and Gerard J Milburn. *Quantum measurement and control*. Cambridge university press, 2009. 8

[40] Patrice Bertet, Irinel Chiorescu, Guido Burkard, Kouichi Semba, CJPM Harmans, David P DiVincenzo, and JE Mooij. Dephasing of a superconducting qubit induced by photon noise. *Physical review letters*, 95(25):257002, 2005. 8

[41] Grégoire Ithier. *Manipulation, lecture et analyse de la décohérence d'un bit quantique supraconducteur*. PhD thesis, Université Paris VI, 2005. 8

[42] David J Griffiths and Darrell F Schroeter. *Introduction to quantum mechanics*. Cambridge University Press, 2018. 10

[43] TP Orlando, JE Mooij, Lin Tian, Caspar H Van Der Wal, LS Levitov, Seth Lloyd, and JJ Mazo. Superconducting persistent-current qubit. *Physical Review B*, 60(22):15398, 1999. 10

[44] KC Gupta, R Garg, I Bahl, and P Bhartia. *Microstrip Lines and Slotlines (Artech House, Norwood, 1996)*. 13

[45] Vinay Ambegaokar and Alexis Baratoff. Tunneling between superconductors. *Physical Review Letters*, 10(11):486, 1963. 20

[46] AJ Ferguson, RG Clark, et al. Energy gap measurement of nanostructured aluminium thin films for single cooper-pair devices. *Superconductor Science and Technology*, 21(1):015013, 2007. 20

[47] *BITL: BILT-BN210 Power Suplyer*. 21

[48] *Keysight: E8257D PSG Microwave Analog Signal Generator menual*. 21

[49] *Narda-MITEQ: SINGLE-POLE SINGLE-THROW SWITCHE datasheet*. 21

[50] *Pulsar-Microwave: AAT-23-479/3S datasheet*. 24

[51] Harry Nyquist. Thermal agitation of electric charge in conductors. *Physical review*, 32(1):110, 1928. 24

[52] *FEMTO Messtechnik GmbH: HVA-500M-20-B voltage amplifier*. 24

[53] JR Sambles, KC Elsom, and G Sharp-Dent. The effect of sample thickness on the resistivity of aluminium. *Journal of Physics F: Metal Physics*, 11(5):1075, 1981. 27

[54] A. A. Clerk and D. Wahyu Utami. Using a qubit to measure photon-number statistics of a driven thermal oscillator. *Phys. Rev. A*, 75:042302, Apr 2007. 33

[55] Simon Gustavsson, Jonas Bylander, Fei Yan, William D Oliver, Fumiki Yoshihara, and Yasunobu Nakamura. Noise correlations in a flux qubit with tunable tunnel coupling. *Physical Review B*, 84(1):014525, 2011. 34

[56] MG Castellano, F Chiarello, P Carelli, C Cosmelli, F Mattioli, and G Torrioli. Deep-well ultrafast manipulation of a squid flux qubit. *New Journal of Physics*, 12(4):043047, 2010. 34

[57] Xiaobo Zhu, Alexander Kemp, Shiro Saito, and Kouichi Semba. Coherent operation of a gap-tunable flux qubit. *Applied Physics Letters*, 97(10):102503, 2010. 34

[58] A Fedorov, AK Feofanov, P Macha, P Forn-Díaz, CJPM Harmans, and JE Mooij. Strong coupling of a quantum oscillator to a flux qubit at its symmetry point. *Physical review letters*, 105(6):060503, 2010. 34

[59] A Fedorov, P Macha, AK Feofanov, CJPM Harmans, and JE Mooij. Tuned transition from quantum to classical for macroscopic quantum states. *Physical review letters*, 106(17):170404, 2011. 34

[60] MJ Schwarz, J Goetz, Z Jiang, T Niemczyk, F Deppe, A Marx, and R Gross. Gradiometric flux qubits with a tunable gap. *New Journal of Physics*, 15(4):045001, 2013. 34

[61] Manuel Johannes Schwarz. *Gradiometric tunable-gap flux qubits in a circuit QED architecture*. PhD thesis, Technische Universität München, 2015. 34

[62] Hui Deng, Yulin Wu, Yarui Zheng, Naheed Akhtar, Jie Fan, Xiaobo Zhu, Jie Li, Yirong Jin, and Dongning Zheng. Working point adjustable dc-squid for the readout of gap tunable flux qubit. *IEEE Transactions on Applied Superconductivity*, 25(3):1–4, 2015. 34

[63] Naheed Akhtar, Yarui Zheng, Mudassar Nazir, Yulin Wu, Hui Deng, Dongning Zheng, and Xiaobo Zhu. Design of a gap tunable flux qubit with fasthenry. *Chinese Physics B*, 25(12):120305, 2016. 34

[64] Yulin Wu, Li-Ping Yang, Ming Gong, Yarui Zheng, Hui Deng, Zhiguang Yan, Yanjun Zhao, Keqiang Huang, Anthony D Castellano, William J Munro, et al. An efficient and compact switch for quantum circuits. *npj Quantum Information*, 4(1):1–8, 2018. 34

[65] David M Pozar. *Microwave engineering*. John wiley & sons, 2009. 35, 36

[66] Kurtis Lee Geerlings. *Improving coherence of superconducting qubits and resonators*. PhD thesis, 2013. 38

[67] Nicholas Adam Masluk. *Reducing the losses of the fluxonium artificial atom*. PhD thesis, 2013. 38

[68] Antonio D Córcoles, Jerry M Chow, Jay M Gambetta, Chad Rigetti, James R Rozen, George A Keefe, Mary Beth Rothwell, Mark B Ketchen, and Matthias Steffen. Protecting superconducting qubits from radiation. *Applied Physics Letters*, 99(18):181906, 2011. 38

[69] DF Santavicca and DE Prober. Impedance-matched low-pass stripline filters. *Measurement Science and Technology*, 19(8):087001, 2008. 38

[70] *EccosorbÂ®MF Lossy Magnetically Loaded Machinable Stock*, 2018. 39

[71] Akio Fukushima, Akira Sato, Akio Iwasa, Yasuhiro Nakamura, Takeshi Komatsuzaki, and Yasuhiko Sakamoto. Attenuation of microwave filters for single-electron tunneling experiments. *IEEE transactions on instrumentation and measurement*, 46(2):289–293, 1997. 41

[72] FP Milliken, JR Rozen, GA Keefe, and RH Koch. 50 ω characteristic impedance low-pass metal powder filters. *Review of Scientific Instruments*, 78(2):024701, 2007. 41

[73] JJA Baselmans and SJC Yates. Long quasiparticle lifetime in aluminum microwave kinetic inductance detectors using coaxial stray light filters. In *AIP Conference Proceedings*, volume 1185, pages 160–163. American Institute of Physics, 2009. 41

[74] *, 2015. 41, 43*

[75] Irena Zivkovic. Dielectric loading for bandwidth enhancement of ultra-wide band wire monopole antenna. Progress In Electromagnetics Research*, 30:241–252, 2012. 41*

[76] JC Maxwell Garnett. Xii. colours in metal glasses and in metallic films. Philosophical Transactions of the Royal Society of London. Series A, Containing Papers of a Mathematical or Physical Character*, 203(359-371):385–420, 1904. 41*

[77] Hsien-Ming Chang, Chungpin Liao, et al. A parallel derivation to the maxwell-garnett formula for the magnetic permeability of mixed materials. World Journal of Condensed Matter Physics*, 1(2):55–58, 2011. 41*

תקציר

קיוביטי השטף נחשבים כאבן בניין המשמש לשם בנייה ויישום של מחשב קוונטי. קיוביט זה בנוי מלולאת אלומיניום דקה, בעלת היקף של מיקרונים בודדים המורכבת מארבע צמתי ג'וזפסון המצטלבים עליה. ניתן להראות כי מעגל זה מתנהג כמערכת שתי רמות, כמעט אידיאלית, כאשר השטף המגנטי החודר דרכה קרוב לחצי מערכו של השטף המגנטי הקוונטי. הנקודה בה ערכו של השטף הוא בדיוק חצי מערכו של שטף המגנטי הקוונטי ידועה בשם הנקודה האופטימלית, הקיוביט מוגן מרעשים בשטף המגנטי וזמן הקוהרנטיות שלו עשוי להגיע לעשרות מיקרו-שניות.

בכדי להרחיב את המערכת למספר רב של קיוביטים, נדרשת שליטה טובה על אנרגיית המעבר של הקיוביט בנקודה האופטימלית. בתזה זו נחליף את אחד מצמתי הג'וזפסון ב-SQUID. הוספת ה-SQUID מאפשרת שליטה וכוונון של אנרגיית המעבר של קיוביטי השטף על פני טווח רחב, אך מקטינה את זמני הקוהרנטיות של הקיוביט אפילו כאשר הוא נמצא בנקודה האופטימלית. על מנת לבטל בעיה זו אנו מציעים להשתמש ב-SQUID לא סימטרי. בכך אנו מגבילים את טווח השליטה על אנרגיית המעבר לתחום יחסית מצומצם, אך שומרים על זמני קוהרנטיות גבוהים.

עבודה זו נעשתה בהדרכתו של ד"ר מיכאל שטרן מהמחלקה לפיזיקה של אוניברסיטת בר-אילן

אוניברסיטת בר אילן

קיוביט שטף ניתן לכוונון בעל זמני קוהרנטיות ארוכים

תמיר כהן

עבודה זו מוגשת כחלק מהדרישות לשם קבלת תואר מוסמך במחלקה לפיזיקה,
אוניברסיטת בר־אילן